PAPER

Check for updates

Fabrication of water-dispersible dye/polymer matrix-stabilized β-FeOOH (Rh-B/F127@β-FeOOH) nanoparticles: synthesis, characterization and therapeutic applications

Neela Mohan Chidambaram, [iD] ‡*[a] Palanisamy Rajkumar,‡[b] P. Arul Prakash,[c] G. M. Rathika,[d] K. Prabhu,[e] Senthil Muthu Kumar Thiagamani, [iD] *[f] M. Khalid Hossain, [iD] *[g] Manikandan Ayyar, [iD] *[h] Lalitha Gnanasekaran[i] and Jinho Kim*[b]

In this study, dye/polymer matrix-stabilized β-FeOOH nanomaterials were fabricated for therapeutic applications. Rh-B/F127@β-FeOOH nanomaterials were synthesized using two different methods: co-precipitation (CoP) and hydrothermal (HT) methods. The as-synthesized nanoparticles were characterized using various spectroscopic techniques, including FT-IR, UV-Vis, PL, XRD, HR-TEM, and XPS analysis. The functional groups and optical properties were confirmed by FT-IR spectroscopy, UV-Vis and fluorescence spectroscopy. The Rh-B/F127@β-FeOOH nanomaterials exhibited both rod-like and sphere-like morphology, as confirmed by HR-TEM analysis. Unlike the nanorods, the nanospheres produced multi-colored emissions at 407, 446, 482 and 520 nm. The oxidative states and elements were confirmed by XPS spectroscopy. MTT assays were used to analyze the cytotoxicity of the nanospheres against A549 cells. The reactive oxygen species (ROS) generation and apoptotic cell death caused by the β-FeOOH nanospheres were evaluated by flow cytometry. Cell cycle analysis indicated that the treatment of nanospheres-induced S-phase cell cycle arrest in A549 cells. The synthesized nanospheres induced late-stage apoptosis in the A549 cell line, with a cell death rate of up to 30.37% at the IC_{50} concentration. Additionally, the antioxidant activities of the synthesized nanorods showed a high scavenging activity against free radicals, as examined by different assays such as such as DPPH, RP, and FRAP. The above results suggest that the synthesized nanorods and nanospheres are promising and efficient material for therapeutic applications.

1. Introduction

Recently, nanomedicines have been developed to boost cancer treatment, creating new potential for improved effectiveness. This is an important breakthrough as cancer is the leading cause of death worldwide. Compared to other cancer types, lung cancer is one of the most frequent malignancies and causes about 19% of deaths worldwide. Nanoparticle research aims to minimize the adverse effects of cancer and allow the precise targeting of tumors without any toxic side effects.[1]

Several research studies have attempted to investigate novel materials with great efficacy and low side effects for cancer

[a]Department of Chemistry, Srimad Andavan Arts and Science College (Autonomous), Affiliated to Bharathidasan University, Tiruchirappalli 620 005, Tamil Nadu, India. E-mail: neela.chem@gmail.com

[b]Department of Mechanical Engineering, Yeungnam University, Gyeongsan-si, 38451, Gyeongbuk, Republic of Korea. E-mail: rajphysics@yahoo.com; jinho@ynu.ac.kr

[c]PG & Research Department of Biotechnology, National College (Autonomous), Affiliated to Bharathidasan University, Tiruchirappalli 620 001, Tamil Nadu, India. E-mail: arulmvp@gmail.com

[d]Department of Chemistry, K. Ramakrishnan College of Technology (Autonomous), Tiruchirappalli 621 112, Tamil Nadu, India. E-mail: gmrathika@gmail.com

[e]PG & Research Department of Biotechnology, Srimad Andavan Arts and Science College (Autonomous), Affiliated to Bharathidasan University, Tiruchirappalli 620 005, Tamil Nadu, India. E-mail: prabhurajk726@gmail.com

[f]Department of Mechanical Engineering, Kalasalingam Academy of Research and Education, Anand Nagar, Krishnankoil, Tamil Nadu, 626126, India. E-mail: tsmkumar@klu.ac.in

[g]Institute of Electronics, Atomic Energy Research Establishment, Bangladesh Atomic Energy Commission, Dhaka 1349, Bangladesh. E-mail: khalid.baec@gmail.com

[h]Department of Chemistry, Centre for Material Chemistry, Karpagam Academy of Higher Education, Coimbatore 641021, Tamil Nadu, India. E-mail: manikandan.frsc@gmail.com

[i]Instituto de Alta Investigación, Universidad de Tarapacá, Arica-1000000, Chile. E-mail: lalitha1887@gmail.com

‡ Neela Mohan Chidambaram and Palanisamy Rajkumar contributed equally to this work.

treatment.[2–4] Combining novel nanomaterials with specific therapeutic technique has shown promise for cancer diagnosis and therapy. However, there are still many challenges to overcome for the development of new materials for use in the preclinical and clinical research of tumors to improve the therapeutic efficacy.[5]

Over the past few decades, nanostructured metal oxide materials have attracted considerable attention due to their distinctive intrinsic characteristics, including tunable surface chemistry, morphology, structure, large surface-volume area, and high chemical stability.[6] Among the various iron-based oxide materials, β-FeOOH (also referred to as akaganeite) with a hollandite-type structure has been utilized as an effective semiconductor, with a band gap of 2.12 eV. The monoclinic crystal-structured akaganeite (β-FeOOH) has a specific gravity (SG) of 3.52 and unit cell parameters of $a = 10.587$ Å, $b = 3.0357$ Å, $c = 10.527$ Å, and $\beta = 90.14$.[7] Its framework is made up of iron oxyhydroxide and includes tunnels that are partially occupied by chloride anions in environments containing chloride.[8] The tunnel structure make it a versatile material that can be used in various areas of applications, like in catalysts, electrodes, ion-exchange materials, and adsorbents.[9–12]

β-FeOOH nanoparticles are commonly synthesized through various methods, like hydrolysis,[13] co-hydrolysis,[14] hydrothermal technique,[15–18] thermolysis,[19] precipitation and co-precipitation method,[20] surfactant-templated synthesis,[21] electric explosion,[22] and green synthesis.[23] Also, nanocrystalline akaganeite exhibits an elevated surface area and a narrow pore-size distribution, showcasing diverse crystal morphologies, such as rod and nanotubes,[17] needles,[21] spindles,[24] and cigar-shaped.[10] The different shapes of β-FeOOH materials have ignited significant research interest regarding their nanoscale derivatives, which have been used in magnetic storage devices, catalysis, and sensors.[25] Besides, low-toxic β-FeOOH nanomaterials have recently been investigated for biological applications, such as MRI (magnetic resonance imaging) for medical diagnosis and therapies.[16,26,27]

The use of organic dyes, like rhodamine-B (Rh-B) and its derivatives, as fluorescent labels has also become prevalent in biological applications due to their excellent physical and chemical properties, such as high fluorescent quantum yield, broad emission wavelength, and sensitivity.[28] However, Rh-B dyes have inherent limitations, such as hydrophobicity, leading to self-bleaching, and poor selectivity, causing the non-specific staining of tissues.[29] To address these issues, researchers have encapsulated Rh-B dyes into biocompatible polymeric carriers to enhance their stability.[30–32] Nonetheless, Rh-B encapsulation within nanoparticles (NPs) often results in aggregation and quenching, even when using polymeric carriers.[33]

One strategy to mitigate aggregation and quenching is by chemically conjugating Rh-B molecules to polymer chains. This approach immobilizes the RB molecules, preventing aggregation and self-quenching. Polymers offer numerous functional groups along their chains, making them suitable for such functionalization or modification.[34] However, many of the polymers that have been explored for this purpose to date lack biocompatibility and have poorly understood toxicity mechanisms.[35]

In the recent past, amphiphilic triblock copolymers, particularly focusing on Pluronic copolymers like Pluronic F-127, have attracted significant attention in various interdisciplinary fields.[36] Pluronic F-127, being a water-soluble triblock copolymer composed of poly(ethylene oxide)–poly(propylene oxide)–poly(ethylene oxide) (PEO–PPO–PEO), possesses several advantageous properties including stability, good mechanical properties, biocompatibility, and a non-toxic nature.[37] Pluronic F-127 has also attracted significant attention due to its ability to serve as a vehicle for drug delivery[38–40] and as a template for nanoparticle synthesis.[41] Due to its biocompatibility, low toxicity against cells and body fluids, and weak immunogenic properties, it is highly suitable for biomedical applications.[37,40]

The aim of this present study was to synthesize high-quality Rh-B/F127@β-FeOOH nanorods and nanospheres for therapeutic applications by two different methods, namely co-precipitation (CoP) and hydrothermal (HT) methods, using dye–micelle (Rh-B/F127) matrix inclusion solutions. The optical, structural, and morphological properties of the obtained Rh-B/F127@β-FeOOH nanoparticles were explored by FT-IR, UV-Vis, PL, XRD, SEM, HR-TEM, and XPS analyses. The synthesized Rh-B/F127@β-FeOOH nanoparticles exhibited good anticancer activities. The cytotoxicity activity of the nanospheres was studied using an MTT assay. For the first time, we demonstrate the Rh-B/F127@β-FeOOH nanospheres-induced apoptosis effect on A549 cells with the help of cell cycle analysis, ROS generation, DAPI, intracellular uptake, and AO/EtBr staining tests. The antioxidant activity of the nanorods was examined by various assays, such as DPPH, RP, and PFRAP assay.

2. Experimental

2.1 Materials

FeCl$_3 \cdot$6H$_2$O ($\geq$98%), FeCl$_2 \cdot$4H$_2$O ($\geq$96%) and urea (98%) were purchased from Merck. Sodium hydroxide (NaOH, 99%) was obtained from LobaChemie. Rhodamine-B (99%) was purchased from Alfa Aesar. The F127 copolymer was purchased from Sigma-Aldrich. All the chemicals were utilized in their original state without any additional purification steps.

2.2 Methods

Rh-B/F127@β-FeOOH nanorods and nanospheres were prepared by co-precipitation (CoP) and hydrothermal (HT) methods using ferric chloride and rhodamine dye/F127 (Rh-B/F127) matrix solutions.

2.2.1 Preparation of urea@β-FeOOH and Rh-B@β-FeOOH nanomaterials

2.2.1.1 Co-precipitation (CoP) method. First, 1 mM of FeCl$_3 \cdot$6H$_2$O and 1 mM urea (acting as fuel) were dissolved in 50 mL of water and heated up to 50 °C for 1 h. Then, the obtained solution was filtered using Whatman No. 40 filter paper to remove the insoluble impurities. Then the solution was heated at 80 °C and maintained at this temperature for 30 min. To this solution,

10 mL of 3 M NaOH solution was added, keeping the pH at 11. After that, the whole solution was maintained at 80 °C for 2 h to allow the growth of β-FeOOH NPs. The prepared NPs were separated by centrifugation and washed with ethanol. To eliminate by-products, the process was repeated at least twice. Finally, the obtained NPs were dried for 3 h at 80 °C.

For the Rh-B@β-FeOOH nanomaterials, 20 mL of rhodamine-B (2.0 mg dissolved in 20 mL water) was initially added instead of urea, followed by the same synthesis procedure as mentioned above.

2.2.1.2 Hydrothermal (HT) method. The synthesis of β-FeOOH nanoparticles was performed by a hydrothermal method without the addition of any precipitating agents. First, 1 mM of $FeCl_3 \cdot 6H_2O$ and 1 mM of urea were dissolved in 50 mL of water, and the solution was heated up to 50 °C and maintained there for 1 h. The obtained solution was then filtered using Whatman No. 40 filter paper. The obtained solution was then transferred to a Teflon-lined stainless-steel autoclave for hydrothermal treatment at 180 °C for 2 h and then cooled down to room temperature. The obtained nanoparticles were separated by centrifugation and washed with ethanol at least twice to remove any by-products. Finally, the obtained nanospheres were dried at 80 °C for 3 h.

For the Rh-B@β-FeOOH nanomaterials, 20 mL of rhodamine-B (2.0 mg dissolved in 20 mL water) was initially added instead of urea, followed by the same protocol as described above.

2.2.2 Preparation of Rh-B/F127@β-FeOOH nanorods and nanospheres

2.2.2.1 Preparation of the dye–micelle inclusion solution. The rhodamine-B/F127 (Rh-B/F127) inclusion matrix solution was initially prepared as follows:[42] first, 1 g of Pluronic F-127 copolymer and 2.0 mg of Rh-B dye were mixed with 100 mL water and then stirred for 2 h to form a dye–polymer inclusion solution.

2.2.2.2 Preparation of Rh-B/F127@β-FeOOH nanorods by the co-precipitation (CoP) method. First, 1 mM of $FeCl_3 \cdot 6H_2O$ was mixed with 50 mL of dye–polymer matrix solution, and then the mixture was heated up to 50 °C and maintained there for 1 h to form a dye–polymer–metal-ion complex. Then, the obtained dye–polymer–metal-ion complex solution was filtered using Whatman No. 40 filter paper to remove any insoluble impurities. Then, 10 mL of 3 M NaOH solution was introduced into the reaction mixture at 80 °C, maintaining the pH at ~11. After that, the whole solution was maintained at 100 °C for 2 h to allow the formation of Rh-B/F127@β-FeOOH nanorods. The prepared NRs were separated using centrifugation and washed with ethanol. To eliminate any by-products, the process was repeated at least twice. Finally, the obtained NPs were dried for 3 h at 120 °C.

2.2.2.3 Preparation of Rh-B/F127@β-FeOOH nanospheres by the hydrothermal (HT) method. The synthesis of Rh-B/F12@β-FeOOH nanospheres was performed by a hydrothermal method without the addition of any surfactant or precipitating agents. In brief, 1 mM of $FeCl_3 \cdot 6H_2O$ was mixed with 50 mL of dye–polymer matrix solution, and the mixture was heated up to 50 °C and maintained there for 1 h to form a dye–polymer–metal-

ion complex. The obtained dye–polymer–metal-ion complex solution was then filtered to remove any insoluble impurities using Whatman No. 40 filter paper. The dye–micelle–metal-ion complex solution was then transferred to a Teflon-lined stainless-steel autoclave and heated at 180 °C for 2 h. The obtained Rh-B/F127@β-FeOOH nanospheres were isolated by centrifugation and washed with ethanol at least twice to remove any by-products. Finally, the obtained nanospheres were dried at 120 °C for 3 h.

2.3 Characterization techniques

Various spectroscopic methods were used to characterize the synthesized Rh-B/F127@β-FeOOH nanorods and nanospheres. UV-visible (Shimadzu) and fluorescence spectroscopy (Shimadzu) were used to investigate the optical (absorption and emission) properties. Infrared spectroscopy (FT-IR) was used to confirm the existence of functional groups in the samples. X-Ray photoelectron spectroscopy (XPS) measurements were performed to determine the phase purity and oxidative states of the elements. To accurately interpret other elemental peaks in the XPS spectrum, C-correction in XPS analysis was applied, which uses the C 1s peak from adventitious carbon on a sample surface as a reference point to calibrate the binding energy scale. This is usually accomplished by setting the C–C bond in the C 1s peak to a standard binding energy of 284.8 eV and aligning all other peaks accordingly. Scanning electron microscopy (SEM) and high-resolution transmission electron microscopy (HR-TEM) were used to examine the surface morphology and particle sizes of the samples. A confocal laser scanning microscope was used for intracellular fluorescence imaging. Flow cytometry (FACSverse Cytometer, Becton, Dickinson and Company (BD)) was used to determine the ratio of cell populations in various cell cycle phases, intercellular uptake, ROS production, and apoptosis cell death.

2.4 Anticancer activity of Rh-B/F127@β-FeOOH nanospheres

2.4.1 Cell viability. The MTT assay was used to determine the cytotoxicity/viability of Rh-B/F127@β-FeOOH nanospheres against the human lung cancer cell (A549) and normal vireo cell (L132) lines, used as models for the cell cytotoxicity assays. In this assay, A549/L132 cells were plated at a density of 1×10^6 cells per well in a 96-well plate at 37 °C in a 5% CO_2 incubator. After 24 h culture, the medium in the wells was replaced with fresh medium with Rh-B/F127@β-FeOOH nanospheres in varying concentrations (0–500 µg). Following 24 h and 48 h incubation periods, 100 µL of a DMEM media solution containing MTT dye (5 mg mL^{-1} in phosphate buffer at pH 7.4) was introduced to each well. Subsequently, 4 h incubation was performed at 37 °C with 5% CO_2, and the culture medium was aspirated, followed by the dissolution of formazan crystals using 100 µL DMSO. The resulting solution was thoroughly mixed to ensure complete dissolution of the reacted dye. The absorbance of each well was measured at 492 nm using a microplate reader. The spectrophotometer was zeroed with a culture medium devoid of cells to provide a baseline. The

relative cell viability (%) compared to control wells containing the cell culture medium was determined using the following formula:[43]

$$\text{Cell viability}(\%) = \frac{AC - AS}{AC} \times 100 \qquad (1)$$

where AC is the absorbance of the control and AS is the absorbance of a sample.

2.4.2 Cellular uptake of nanospheres using DCFH-DA staining. The accumulation of intracellular reactive oxygen species (ROS), including free radicals, was assessed in A549 cells using dichlorodihydrofluorescein diacetate (DCFH-DA) staining. To perform this analysis, we initially seeded 105 cells per well in 6-well plates and allowed them to grow overnight. Subsequently, the cells were incubated with Rh-B/F127@β-FeOOH nanospheres for a period of 24 h. After removing the medium, the cells were washed with PBS and stained in the dark at room temperature with 100 µL of DCFH-DA (50 µM) for 10–15 min. The resulting fluorescence was observed under a fluorescence microscope (Olympus CKX53) at 20× magnification.

2.4.3 Cell cycle analysis using flow cytometry. The A549 cell line was initially cultured in 6-well plates using a high-glucose DMEM medium. After a certain incubation period, the cells achieved optimal growth and were subsequently exposed to Rh-B/F127@β-FeOOH nanospheres for 24 h treatment. After the 24 h treatment, the cells were trypsinized and resuspended in complete media. The resulting cell pellet was washed twice with PBS and subsequently fixed by incubating it with 1 mL of 70% ice-cold ethanol overnight at 4 °C. After removing the ice-cold ethanol, the cell pellet was washed twice with cold PBS, and then added to 10 µL of RNase A 10 g mL^{-1} and incubated for 30 min, followed by washing with PBS. The cells were then resuspended in 1 mL of PBS together with 50 µL propidium iodide (1 mg per mL stock) for 30 min in the dark. Next, the cells underwent analysis by flow cytometry (FACSverse Cytometer, BD) to determine their cell cycle phase.

2.4.4 ROS generation. A549 cells were treated with Rh-B/F127@β-FeOOH nanospheres in high-glucose DMEM media in a 6-well plate for 24 h. Afterwards, the cells were trypsinized, pelleted, and then added to 50 µL of 10 µm DCF-DA (Sigma-Aldrich) and kept under incubation in the dark for 30 min. Finally, flow cytometry (FACSVerse Cytometer, BD) was used to measure the ROS levels in the cells.

2.4.5 Apoptosis. Apoptosis detection was performed using the FITC Annexin-V with PI (Apoptosis Detection Kit, BD Biosciences USA) protocol. A549 cells, a lung cancer cell line, underwent 24 h treatment with Rh-B/F127@β-FeOOH nanospheres in high-glucose DMEM media. Following the treatment, the cells were trypsinized, suspended in PBS, subjected to two washes, and then centrifuged to remove the PBS. The cells were then suspended in 100 µL of binding buffer, and then stained with 5 µL of annexin-V and propidium iodide for 15 min incubation in the dark at room temperature following the protocol advised by the flow cytometer manufacturer's instructions (cat no. 556547). The diluted cells, stained with 450 µL of binding buffer, were

examined by flow cytometry (FACSverse Cytometer, BD), and the data were subsequently analyzed with FACSverse software.

2.4.6 DAPI staining. Fluorescence microscopy was employed to visualize the morphologies of the cell nuclei using the simple fluorescent stain 4′,6-diamidino-2-phenylindole (DAPI). The A549 cells were treated with Rh-B/F127@β-FeOOH NPs for 24 h. Then the cells were washed using PBS (pH 7.4) and fixed with ice-cold paraformaldehyde. After that, the cells further washed using PBS (pH 7.4) followed by the addition of DAPI and then incubation for 15 min at 37 °C and wrapped in aluminum foil. The cells were examined under an Olympus CKX53 fluorescence microscope to observe the staining pattern.

2.4.7 Apoptosis induction analysis by dual AO/EtBr staining assay. The apoptotic effect of Rh-B/F127@β-FeOOH nanoparticles on A549 cells was verified by acridine orange/ethidium bromide (AO/EB) staining, in accordance with a methodology previously outlined.[44] The Rh-B/F127@β-FeOOH NP-treated cells were examined morphologically for indications of apoptosis using AO/EB staining. In brief, 5 × 105 A549 cells were seeded on a cover slip in a 6-well plate, and then exposed to nanoparticles at the proper IC$_{50}$ concentration. After removing the cover slips from the plate, they were treated with 10 µL mL^{-1} of AO (10 mg mL^{-1}) and EB (10 mg mL^{-1}) and cleaned again with 1× PBS buffer. Using 1× PBS buffer, unbound dye was eliminated following a 15 min incubation period. Using an excitation filter set at 480 nm, representative fields of the cells were photographed at 40× magnification for examination under a fluorescent microscope.

2.5 *In vitro* antioxidant assays of Rh-B/F127@β-FeOOH nanorods

2.5.1 DPPH free-radical-scavenging assay. The antioxidant activity of Rh-B/F127@β-FeOOH nanorods was screened using the modified DPPH method as reported by Serpen *et al.* (2007).[45] Briefly, a stock solution (10 mg mL^{-1}) of Rh-B/F127@β-FeOOH nanorods and standard L-ascorbate solutions were prepared and diluted to the desired concentrations. Different concentrations (100, 200, 300, 400, and 500 µg mL^{-1}) of Rh-B/F127@β-FeOOH nanorods were added to 10 mL of 0.1 mM 2,2-diphenyl-1-picrylhydrazyl (DPPH) solution and then incubated in the dark for at least 30 min at room temperature. The mixture was centrifuged for 2 min, and finally, the absorbance was analyzed at 517 nm using a UV-Vis spectrophotometer. The antioxidant activity was calculated by a DPPH radical scavenging assay using the following formula:

$$\text{Scavenging}(\%) = \frac{AC - AS}{AC} \times 100 \qquad (2)$$

where AC is the absorbance of the control sample (DPPH) and AS is the absorbance of a sample with DPPH. Additionally, 0.1 mM DPPH and L-ascorbate were used as a control and standard solution.

2.5.2 Reducing power assay. With a minor modification, the method established by Pulido *et al.* (2000)[46] was used to determine the reducing power of the nanorods. Five different nanorods doses (100, 200, 300, 400, and 500 g mL^{-1}) were mixed with 1 mL of potassium ferricyanide (K$_3$Fe(CN)$_6$) (1%, w/v) and

1 mL of phosphate buffer (2 mM, pH 6.6). The mixture solutions were then incubated at 50 °C in an incubator for 20 min. The reaction was completed by adding 1 mL of 10% (w/v) trichloroacetic acid (TCA) after centrifugation at 3000 rpm for 15 min. The supernatant solution (1.5 mL) was combined with 1.5 mL of distilled water and 0.1 mL of a 0.1% (w/v) ferric chloride (FeCl$_3$) solution, and the mixture was stirred for 10 min. Then, the absorbance was subsequently measured at 700 nm in comparison to a blank solution. An elevated absorbance measurement in the reaction mixture indicated a greater degree of reducing power. Three replicates of each sample were measured, and the average was recorded. Ascorbic acid was used as a standard. To ascertain their reducing power, the absorbance values of the samples were related to that of the standard ascorbic acid.

2.5.3 Ferric reducing antioxidant power (FRAP) assay. A ferric reducing antioxidant power (FRAP) assay was performed for the Rh-B/F127@β-FeOOH nanorods following a previously reported method.[47] Briefly, a stock FRAP solution was formulated through the combination of 10 mM TPTZ (2,4,6-tripyridyl-s-triazine), 300 mM acetate buffer (consisting of 3.1 g of sodium acetate trihydrate and 16 mL of acetic acid, adjusted to a pH of 3.6), and 20 mM ferric chloride hexahydrate in a 40 mM HCl solution. Different concentrations of nanorods (0.5 mL) were individually placed into distinct test tubes, and 4.5 mL of the FRAP reagent was introduced to reach a final volume of 5 mL. The mixture was then incubated at 37 °C for 30 min. Finally, the absorbance was recorded at a wavelength of 593 nm. The formation of a dark blue color indicated that the TPTZ–Fe^{3+} complex was reduced to TPTZ–Fe^{2+} by the antioxidant.

3. Results and discussion

3.1 Formation of dye/copolymer matrix-stabilized β-FeOOH NPs

We developed rhodamine-B/F127 polymer matrix-stabilized β-FeOOH (Rh-B/F127@β-FeOOH) nanorods and nanospheres by co-precipitation and hydrothermal methods. To synthesize Rh-B/F127@β-FeOOH nanorods, a co-precipitation approach was conducted. In this reaction system, NaOH solution was introduced into the reaction mixture at 80 °C. The color of the mixture suddenly changed from light pink to yellowish-brown, and then the temperature increased to 100 °C to form a dark-brown precipitate, which indicated the formation of an iron oxyhydroxide (β-FeOOH) colloidal suspension. Eqn (3) depicts the synthesis route for the Rh-B/F127@β-FeOOH nanorods.[48]

$$Fe^{3+} + 3OH^- \rightarrow Fe(OH)_3 \rightarrow FeOOH + H_2O \quad (3)$$
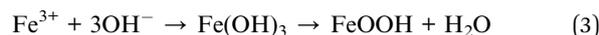
Also, a simple hydrothermal approach was used to synthesize Rh-B/F127@β-FeOOH nanospheres at a high temperature (180 °C) for 2 h. In this reaction, no precipitating agents were used. The chemical reaction that occurred in this reaction can be represented as follows (eqn (4)):[49]

$$Fe^{3+} + 2H_2O \rightarrow FeOOH + 3H^+ \quad (4)$$

Scheme 1 shows a schematic representing the synthesis routes for the Rh-B/F127@β-FeOOH nanomaterials using co-precipitation (CoP) and hydrothermal (HT) methods.

3.2 Fourier-transform infrared (FT-IR) analysis

The capping of the dye/copolymer matrix and its interaction with the surface of β-FeOOH NPs was performed for the FT-IR spectroscopy investigations. The presence of functional group over the surface of the pure β-FeOOH nanoparticles was confirmed using the FT-IR bands Fig. 1(a) and (b) displays the FT-IR spectra of β-FeOOH, Rh-B@β-FeOOH, and Rh-B/F127@β-FeOOH nanoparticles.

Fig. 1(a1) and (b1) shows the presence of functional groups over the surface of β-FeOOH nanoparticles, as confirmed by the FT-IR bands at ~3440, ~1630, ~1450, ~820, and ~620 cm^{-1}. The bands at ~3450 cm^{-1} corresponded to the presence of N–H stretching modes in amide groups. The absorption peak around 1655 cm^{-1} represented the C=O stretching of the amide, while C–N stretching frequency appeared at 1450 cm^{-1}. The FT-IR bands at ~1600 cm^{-1} were ascribed to the –OH stretching vibration, while the bands at 922 and 620 cm^{-1} were ascribed to the –OH bending modes in β-FeOOH.[50] The FT-IR spectrum indicated that the urea was coordinated with the β-FeOOH nanorods surface through the oxygen atom of the C=O group or the nitrogen atom of the N–H group, resulting in the formation of urea-capped β-FeOOH nanoparticles.

Several specific absorption bands appeared in the FT-IR spectra of the rhodamine-B capped β-FeOOH nanorods. As shown in Fig. 1(a2) and (b2), the intense peaks at ~1410 cm^{-1} corresponded to the asymmetric and symmetric C–N stretches. The appearance of an intense peak may be due to the large dipole moment of carboxylate. The bands at ~3420 cm^{-1} were ascribed to the existence of N–H stretching. The appearance of bands at ~1630 cm^{-1} was attributed to the –OH stretching vibration, while the bands at 840 and 626 cm^{-1} were ascribed to the –OH bending modes in β-FeOOH.[50] The overall results confirmed the formation of Rh-B-capped β-FeOOH NPs.

In order to prove the conjugation of the dye/polymer matrix over the β-FeOOH NPs, FT-IR was carried out. Fig. 1(a3) and (b3) clearly shows the presence of a peak located at ~1100 cm^{-1}, which was accredited to the stretching vibration of C–O–C in the polymer chain of the F127 copolymer, and was ascribed to the newly formed ester bond between the F127 copolymer and Rh-B dye. In addition, the absence, as shown in Fig. 1(a2) and (b2), of a band at 1450 cm^{-1} confirmed the formation of the Rh-B/F127 polymer matrix. The presence of a broadband at ~3620 cm^{-1} was accredited to the stretching vibration of –OH groups in the F127 polymer. The characteristic peaks at 650 cm^{-1} corresponded to the Fe–O stretching vibration mode in β-FeOOH.[50] These findings confirmed the formation of Rh-B/F127@β-FeOOH NPs containing both Rh-B and F127 copolymer, as predicted by the preparation process.
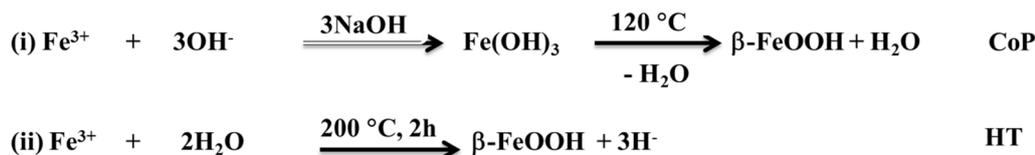
3.3 UV-Vis analysis

The absorption spectra of the synthesized β-FeOOH, Rh-B@β-FeOOH, and Rh-B/F127@β-FeOOH nanomaterials are shown in
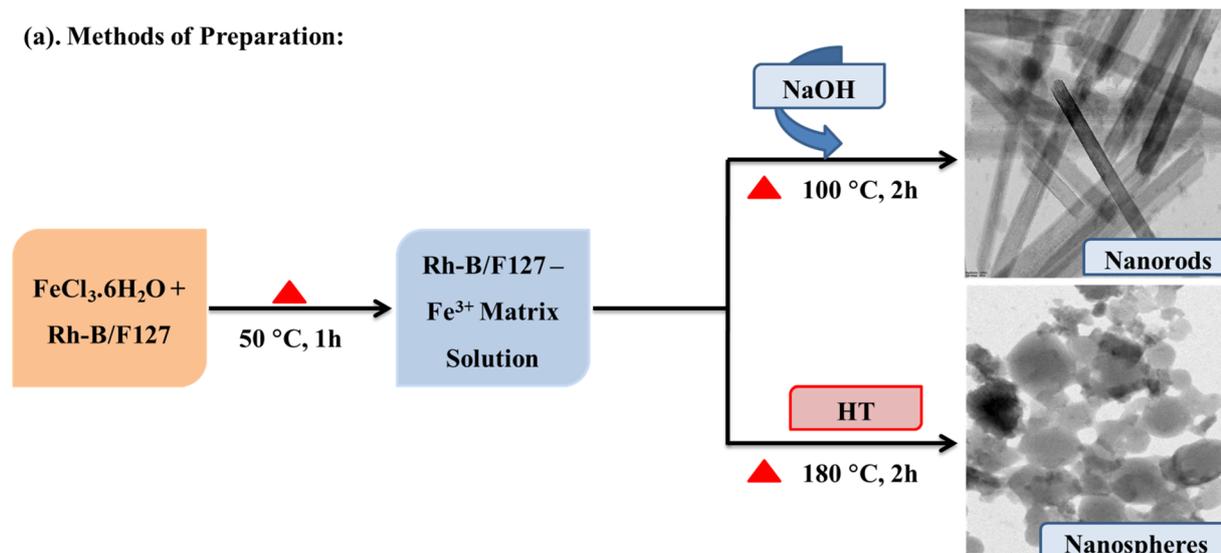
Scheme 1 Schematic diagram of the synthesis routes for β-FeOOH nanoparticles. (a) Synthesis of β-FeOOH nanomaterials by co-precipitation (CoP) and hydrothermal (HT) methods; the corresponding TEM images confirm the rod-like and spherical-like morphologies. (b) Proposed mechanisms for the formation of β-FeOOH nanorods and nanospheres.
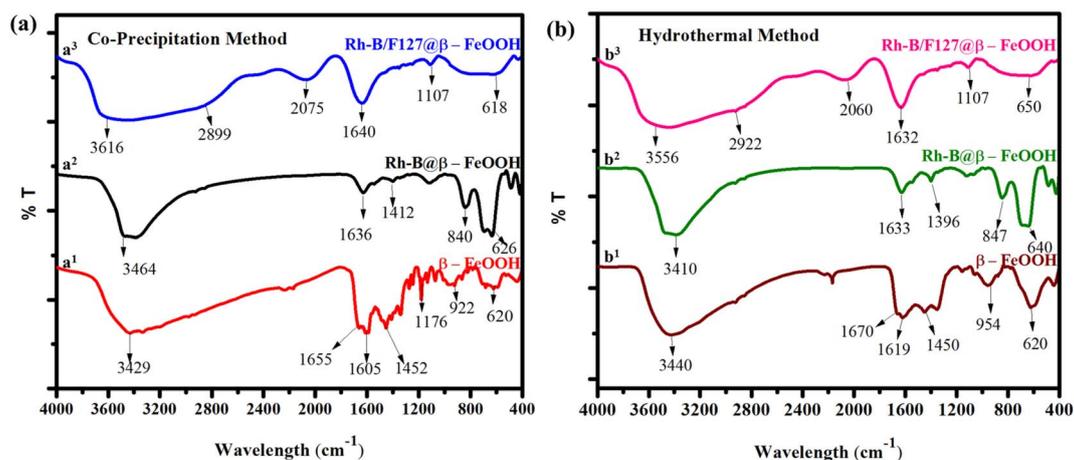

Fig. 1 FT-IR spectra of β-FeOOH NPs prepared by (a) co-precipitation and (b) hydrothermal methods; (a[1] and b[1]) urea-capped β-FeOOH NPs, (a[2] and b[2]) Rh-B@β-FeOOH, and (a[3] and b[3]) Rh-B/F127@β-FeOOH NPs.

Fig. 2. As can be seen in Fig. 2(a1) and (b1), an onset absorption band can be clearly observed in the visible region. This result is consistent with data from other studies.[11] In both cases, the absorption peaks of Rh-B and the Rh-B/F127-capped β-FeOOH nanomaterials were blue-shifted compared to the pristine β-FeOOH nanoparticles. The appearance of the blue-shift may be due to the formation of β-FeOOH NPs by the dye/copolymer matrix. The band gap (E_g) for the synthesized samples was

ascertained by extrapolation from the absorption edge, which is given by the following equation:[51]

$$(\alpha h\nu)^n = A(h\nu - E_g) \qquad (5)$$

where α is the absorption coefficient, A is a constant, $h\nu$ is the energy of light, and n is a constant depending on the electron transition. Fig. 2(a2) and (b2) display a plot of $(\alpha h\nu)^2$ versus $h\nu$. The energy gap, E_g, was determined by finding the point where
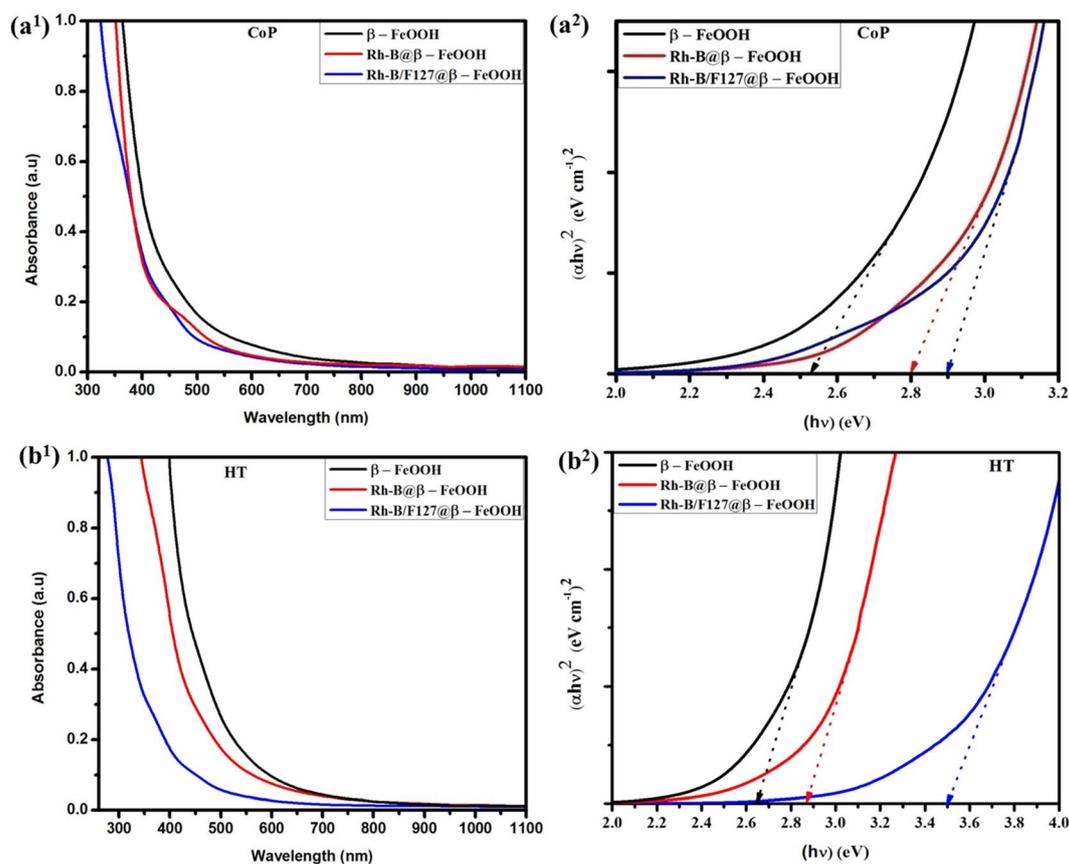
Fig. 2 (a^1 and b^1) UV-Vis spectra and (a^2 and b^2) bandgaps of the Rh-B/F127@β-FeOOH nanorods and nanospheres. The bandgap of the nanoparticles was calculated by the Tauc equation. The optical bandgaps were obtained by extrapolating the linear portion of $(\alpha h\nu)^2$ *versus* $h\nu$ and were found to be between 2.52 and 3.50 eV.

the linear absorption edge intersected the energy axis, specifically when $(\alpha h\nu)^2$ equals zero. Table 1 shows the bandgaps of the synthesized nanomaterials. The bandgap of the as-synthesized nanoparticles was found to vary between 2.52 and 3.50 eV. The decrease in particle size, difference in crystallinity, or shape-dependent properties may be responsible for increasing the optical bandgap of the β-FeOOH nanoparticles.

3.4 Photoluminescence analysis

The PL spectra of the synthesized β-FeOOH nanoparticles were recorded at an excitation wavelength of 360 nm and the corresponding emission spectra are shown in Fig. 3. The synthesized nanorods displayed three different emissions with lower

Table 1 Bandgaps of the synthesized Rh-B/F127@β-FeOOH nanorods and nanospheres

		Bandgap (eV)	
S. no.	Samples	Nanorods	Nanospheres
1	β-FeOOH	2.52	2.60
2	Rh-B@β-FeOOH	2.80	2.86
3	Rh-B/F127@β-FeOOH	2.90	3.50

intensities located at 437, 477, and 518 nm, respectively and their respective spectra are presented in Fig. 3(a).

Unlike the nanorods, the nanospheres emitted five different emissions at 360, 407, 446, 482 and 520 nm upon excitation at the 320 nm wavelength (Fig. 3(b1) and (b2)). The existence of an emission peak at 360 nm (due to UV emission) may be related to the recombination of electron–hole pairs in the free excitons.[52] The emission bands located at 407, 446, 482, and 520 nm led to violet, deep-blue, a deep greenish-blue (cyan color), and green emissions, respectively. The emission peak that appeared at 407 nm may be due to LMCT related to the HOMO of the ligand and the LUMO centered over Fe^{3+} metal ions.[53] The other peaks at 446, 482, and 520 nm could be ascribed to (i) $^6A_{1g} \rightarrow \,^4T^{1g}$ and $^6A^{1g} \rightarrow \,^4T_{2g}$ transitions involving d–d orbitals of Fe^{3+} ions, and may be to the crystal field splitting of a FeO_6 octahedron with an O_h symmetry[54,55] or (ii) ligand effects between the ligand functional groups and Fe^{3+} centers at the NPs' surfaces.[56]

In addition, compared to the fluorescence spectra of Rh-B@β-FeOOH nanoparticles, the Rh-B@F127 matrix-stabilized β-FeOOH NPs exhibited slightly higher emission intensities with 2–4 nm blue-shifts. This phenomenon may be attributed to either (i) surface modification by the growth of the Rh-B/F127 matrix over the surfaces of the β-FeOOH nanoparticles, which may reduce the sizes of the nanomaterials, or (ii) the interaction
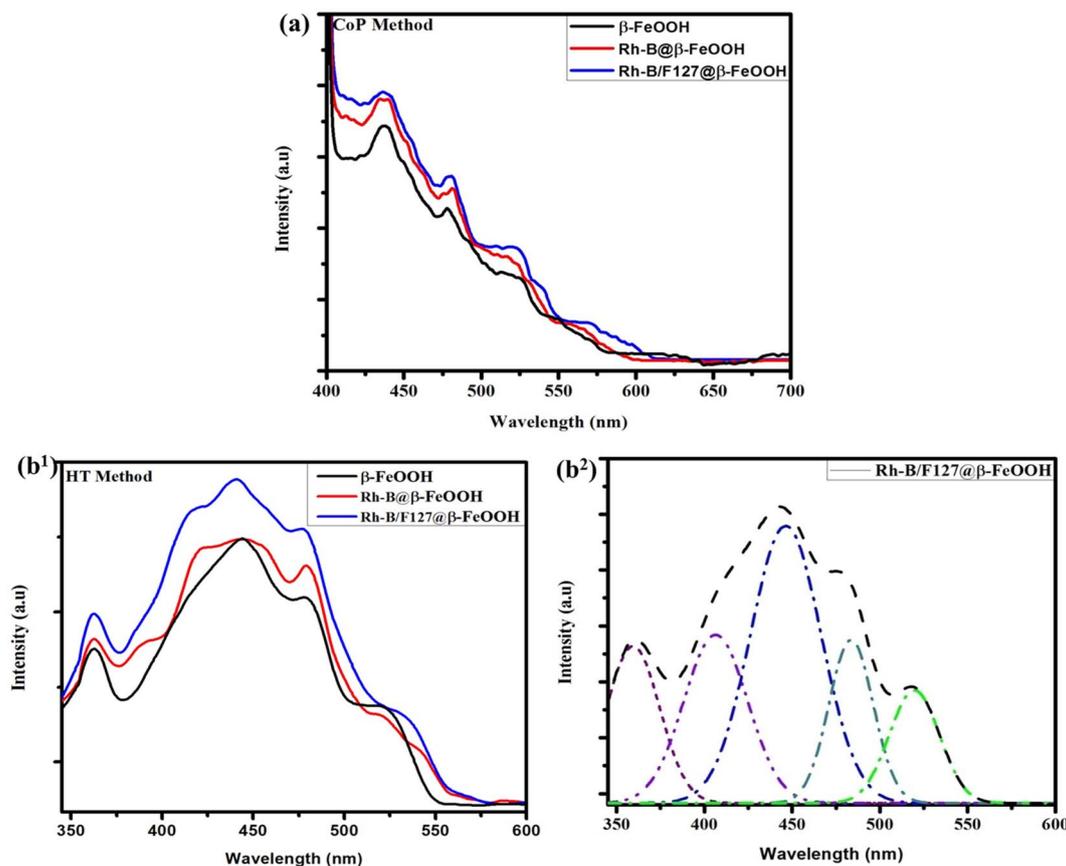
Fig. 3 (a) PL spectra of β-FeOOH nanorods using an excitation wavelength of 380 nm, (b^1) PL spectra of β-FeOOH nanospheres using an excitation wavelength of 320 nm; and (b^2) Gaussian band deconvolution of the PL spectra of the Rh-B/F127@β-FeOOH nanospheres.

between the dye/F127 matrix and the internal surface of the β-FeOOH nanoparticles which may increase electron–hole recombination over the surfaces of the β-FeOOH NPs.

3.5 XPS analysis

XPS analysis confirmed the oxidation states and elemental compositions of the Rh-B/F127@β-FeOOH nanospheres. The core-level XPS spectra and their corresponding energy levels are presented in Fig. 4(a)–(f). The survey spectrum (Fig. 4(a)) showed the presence of Fe 2p, O 2p, and C 1s peaks. As shown in Fig. 4(c), the Fe 2p core was split into Fe $2p_{3/2}$ and Fe $2p_{1/2}$ peaks. The binding energies of Fe $2p_{3/2}$ and Fe $2p_{1/2}$ were located at 712 and 726 eV, respectively, which were in good agreement with the reported literature for β-FeOOH.[15,57,58] Small shake-up satellite peaks at 718.9 and 733.4 eV could also be detected in the XPS spectra, which were characteristic of Fe^{3+} in the octahedral sites of the synthesized β-FeOOH nanospheres.[16] As shown in Fig. 4(b), the presence of C 1s was shown by a peak that appeared at 283 eV due to the presence of rhodamine-B and the F127 matrix over the β-FeOOH nanospheres. From Fig. 4(d), the presence of oxygen atoms was further confirmed from the O 1s core-level spectrum, with two bands appearing at 530.1 and 531.5 eV, which were assigned to Fe–O–Fe and Fe–O–H bonds, respectively.[59] The above result indicates that the oxidation state of oxygen in the present case was −2. The XPS spectrum of Fe 3p

is shown in Fig. 4(e). From Fig. 4(f), the binding energy of Cl 2p at 200.00 eV suggested the presence of Cl atoms, which would be located in the hollandite channels of β-FeOOH.[60] The XPS results provide evidence for the formation of Rh-B/F127@β-FeOOH nanospheres with hollandite structures. The binding energies, oxidation states, and percentage compositions of the elements present in the nanospheres are listed in Table 2.

3.6 Crystal structural analysis

X-Ray diffraction analysis (XRD) was used to further confirm the crystal structures of the as-produced nanorods and nanospheres, and the corresponding XRD patterns are shown in Fig. 5(a) and (b). Obviously, all the diffraction peaks of the prepared sample were in good agreement with the reference data for the β-FeOOH phase.[20] The peaks appearing at $2\theta =$ 11.81°, 16.71°, 26.50°, 33.75°, 34.95°, 38.95°, 46.07°, 52.01°, 55.71°, 61.20°, 64.18°, and 68.58° could be ascribed to the (110), (200), (130), (400), (211), (301), (411), (600), (251), (002), (541), and (132) reflection planes.[61] The observed peaks aligned with the tetragonal structure of the pure β-FeOOH phase (JCPDS 34-1266) and thus could be accurately indexed. There were no additional peaks from other phases, like Fe_2O_3, or Fe_3O_4, observed. The absence of peaks from other iron oxide phases suggested that the synthesized β-FeOOH nanoparticles were successfully prepared without any impurities. The widening of

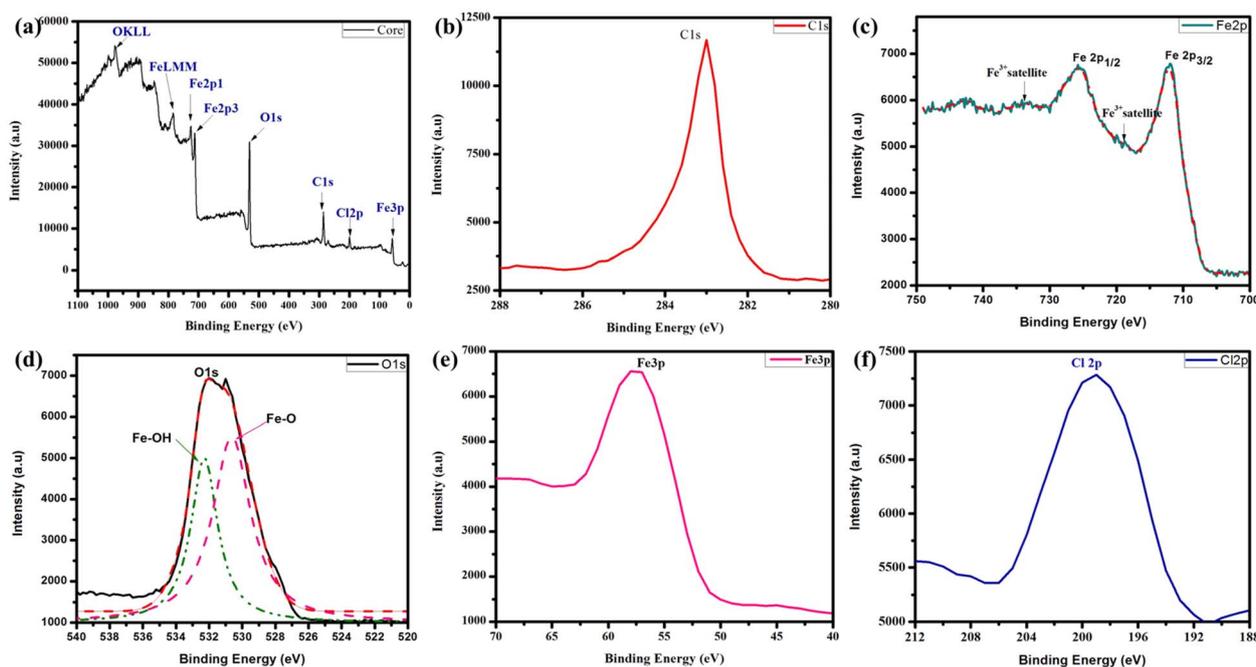Fig. 4 (a–f) XPS spectra of the Rh–B/F127-matrix-stabilized β-FeOOH nanospheres; (a) XPS survey spectrum; (b) XPS spectrum of C 1s; (c) XPS spectrum of Fe 2p; (d) XPS spectrum of O 1s. (e) XPS spectrum of Fe 3p and (f) XPS spectrum of Cl 2p.

Table 2 Binding energies, oxidation states, and % composition (atomic%) of the Rh–B/F127@β-FeOOH nanospheres

S. no.	Core-levels	Splitting	Binding energy (eV)	Splitting width (eV)	Oxidation state	% composition (at%)
1	Fe 2p	Fe 2p3/2	712.0	13.0	+3	20.6
		Fe 3p1/2	725.0			
2	O 1s	O 1s (Fe–OH)	532.0	2.0	−2	78.3
		O 1s (Fe–O)	530.0			
3	C 1s	—	283.0	—	—	—
4	Cl 2p	—	200.0	—	—	1.1

the diffraction peaks further confirmed that the nanoparticles had nanocrystalline structures, indicating their small size and high surface area.

The approximate crystallite size "*D*" of the synthesized nanoparticles was estimated using the following Scherrer's equation:[62]
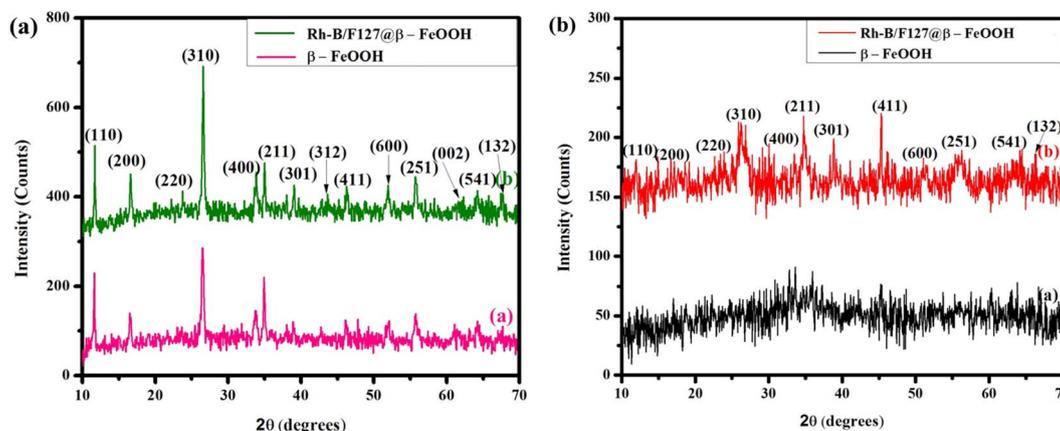

Fig. 5 XRD patterns of β-FeOOH and Rh–B/F127@β-FeOOH nanoparticles synthesized by (a) CoP and (b) HT methods. The observed peaks well matched with the tetragonal structure of the β-FeOOH phase and JCPDS card no. 34-1266.

$$D = \frac{k\lambda}{\beta \cos\theta} \tag{6}$$

where k is the so-called shape factor (0.9), λ is the wavelength (0.15418 nm, CuKα), β is the full width at half maximum (FWHM), and θ is the diffraction angle. From the XRD patterns, we could estimate the average size of the nanospheres as 45 ± 2 nm. The average crystallite size obtained by XRD was very close to that obtained from the TEM results, indicating a high level of agreement between the two techniques.

3.7 HR-TEM analysis

HR-TEM analysis was next used to investigate the morphology and size of the nanoparticles. Fig. 6 shows the HR-TEM images of the as-obtained Rh-B/F127@β-FeOOH nanomaterials synthesized using co-precipitation and hydrothermal methods. The typical TEM image (Fig. 6(a1), synthesized by CoP) displayed a rod-like morphology with widths of 17–20 nm and lengths of 0.5–1.0 μm. The SAED pattern of single nanorods is shown in Fig. 6(a3). The alignment of bright spots in parallel affirmed the single-crystalline nature of the nanorods. In addition, clear lattice fringe could be observed from Fig. 6(a2), which revealed the single-crystalline nature of the samples. The interplanar distance measured approximately 0.511 nm, aligning with the d-spacing observed in the (200) plane of β-FeOOH.

As shown in Fig. 6(b1), the TEM images revealed that the hydrothermally prepared β-FeOOH nanoparticles were nearly spherical in morphology with an average diameter of 45.0 nm, which was very close to the crystallite size (nm) calculated from the XRD pattern. Fig. 6(b3) shows the SAED pattern of the

nanospheres, indicating the high crystallinity of the β-FeOOH NPs. Fig. 6(b2) clearly illustrates the interatomic separation was 0.470 nm, which was good agreement with the interatomic separation in the (101) plane.

3.8 Anticancer activity of the Rh-B/F127@β-FeOOH nanospheres

To the best of our knowledge, no study has yet evaluated the anticancer activity against Rh-B/F127@β-FeOOH nanospheres. Here, we aimed to evaluate the potential anticancer activity of β-FeOOH nanospheres against A459 cells. Flow cytometry was used to investigate the cellular uptake, cell cycle arrest, ROS generation, and apoptotic cell death, by Rh-B/F127@β-FeOOH nanospheres using annexin-V and propidium iodide (PI) staining.

3.8.1 *In vitro* cytotoxicity activity analysis. To determine the potential for biomedical applications of the synthesized Rh-B/F127@β-FeOOH nanospheres, the cytotoxicity of the synthesized materials was evaluated by exposing them to cultured human lung cancer cells (A549) and a normal cell line (L132). Cytotoxicity studies can greatly help to assess the utility of synthesized nanoparticles as an efficient material in cancer treatments. The MTT assay was studied to determine the cell viability of the A549 and L132 cell lines.

The A549 and L132 cells were treated with various concentrations ranging from 0–500 μg mL^{-1} for 24 and 48 h. The concentration-dependent cell viabilities are shown in Fig. 7, which clearly indicate that the cell viability decreased with increasing the nanoparticles' concentration. As can be seen in Fig. 7, the L132 cells displayed more than 80% cell viability at
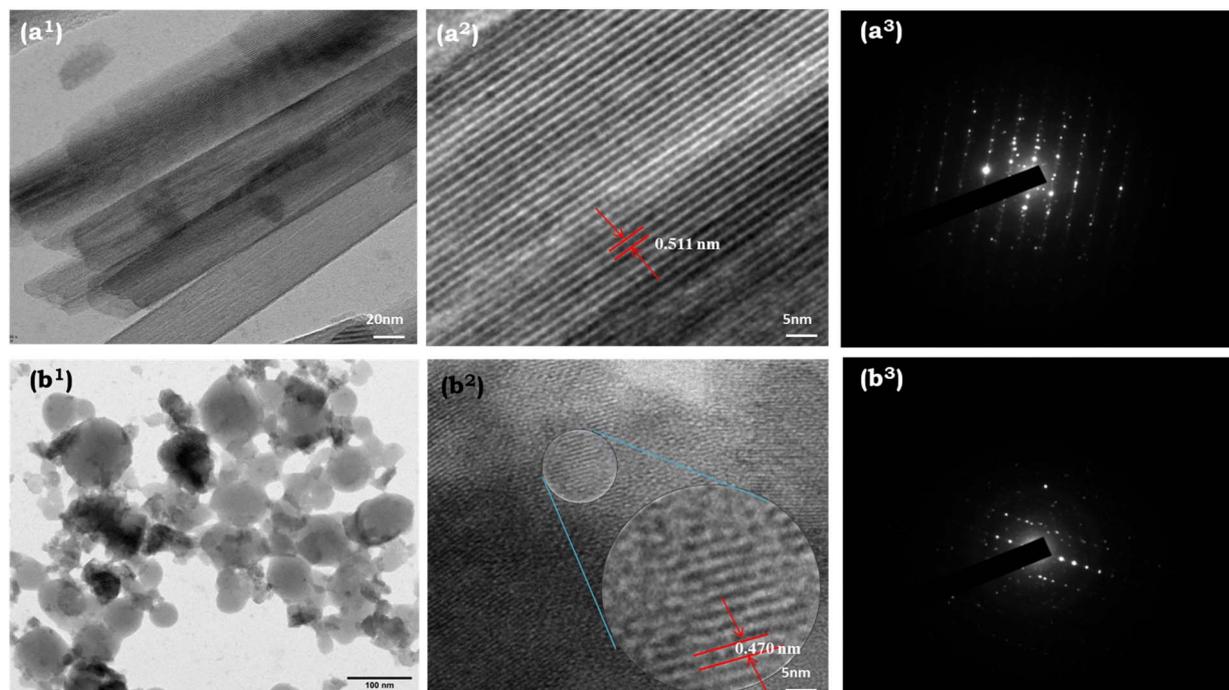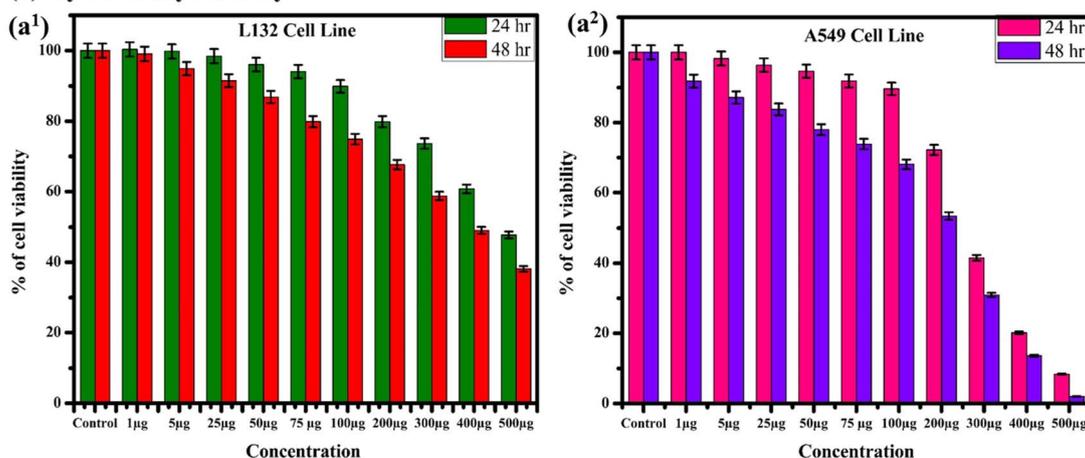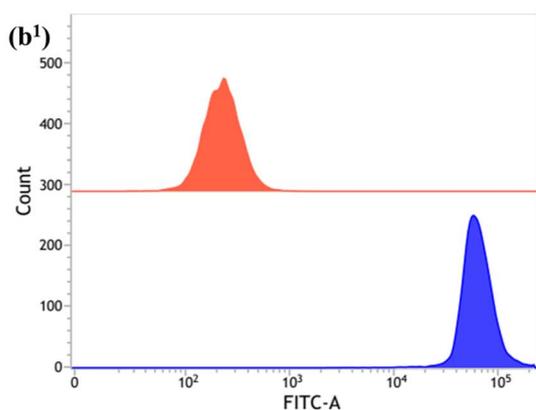

Fig. 6 HR-TEM micrographs of the Rh–B/F127@β-FeOOH nanomaterials prepared by (a) CoP and (b) HT methods. (a¹ and b¹) TEM images showing the nanorods- and nanospheres-like morphologies of Rh–B/F127@β-FeOOH nanoparticles; (a² and b²) interplanar spacings, and (a³ and b³) SAED patterns of the Rh–B/F127@β-FeOOH nanorods and nanospheres.
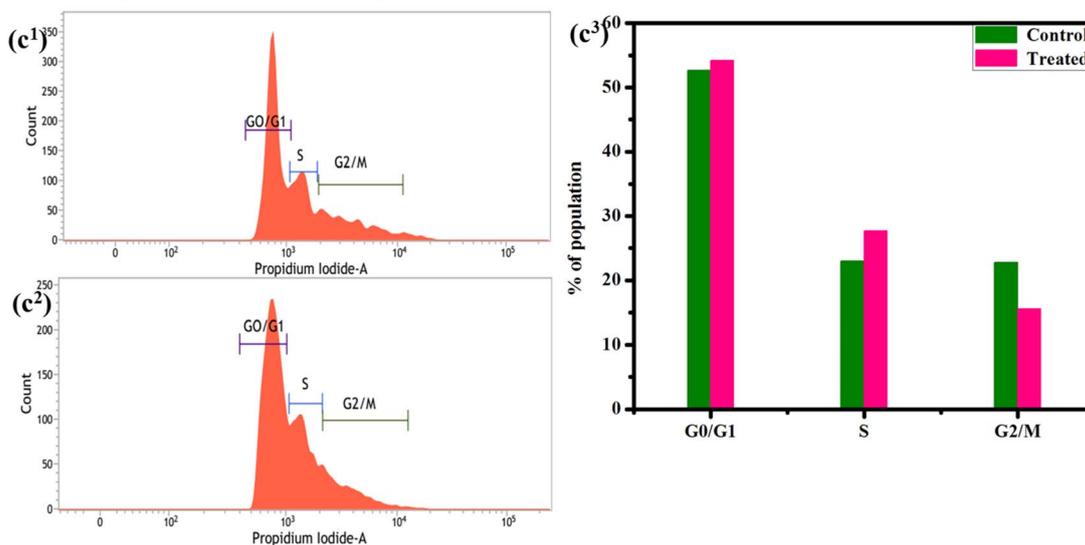
Fig. 7 Cytotoxicity analysis. (a) Cytotoxicity activities: (a^1) L132 cell line and (a^2) A549 cell lines at 24 and 48 h treatment with Rh–B/F127@β-FeOOH nanospheres as revealed by MTT assay. (b). Cellular uptake analysis: (b^1) flow cytometry quantification of Rh–B/F127@β-FeOOH nanospheres uptake by A549 cells. (c). Cell cycle distribution analysis: representative histograms showing the cell population according to the DNA content as determined by propidium iodide staining. (c^1) Control and (c^2) treated cells with Rh–B/F127@β-FeOOH nanospheres; (c^3) bar diagram of cell distribution in the G0/G1, S, and G2/M phases. The results indicated that the nanoparticles-induced cell cycle arrest in the S phase.

300 μg mL^{-1} for 24 h (Fig. 7(a1)) after being exposed to Rh-B/F127@β-FeOOH nanospheres, whereas the A549 cells showed less than 45.0% cell viability (Fig. 7(a2)). The calculated IC$_{50}$ concentration of Rh-B/F127@β-FeOOH nanospheres was 260 μg mL^{-1}. Previous studies have investigated the cytotoxicity of iron oxide nanoparticles and their nanocomposites. For instance, Bhushan et al. (2018) demonstrated that α-Fe$_2$O$_3$/Co$_3$O$_4$ nanocomposites exhibited greater toxicity than α-Fe$_2$O$_3$ toward MCF-7 cells after 24 h,[63] while Alkinani et al. (2024) demonstrated that Fe$_3$O$_4$@Glu–gingerol NPs displayed selective cytotoxicity, with a markedly lower IC$_{50}$ value in A549 cancer cells (190 μg mL^{-1}) versus normal cells (554 μg mL^{-1}).[64] Another study reported that iron oxide nanoparticles showed 50% viability in A549 cells at a concentration of 970 μg mL^{-1} after 24 h.[65] In contrast, our result showed that the Rh-B/F127@β-FeOOH nanospheres achieved 50% viability in A549 cells at a significantly lower concentration of 260 μg mL^{-1}. These findings suggested that the Rh-B/F127@β-FeOOH nanospheres hold promise as a cytotoxic agent against cancer cell lines. The above results confirmed that the hydrothermally synthesized nanospheres have good biocompatibility and can be used as a therapeutic agent.

3.8.2 Cellular uptake of Rh-B/F127@β-FeOOH nanospheres. For quantification of the nanoparticle uptake and intracellular distribution by human lung cancer cells (A549 cell line), we adopted a flow cytometry approach. Fig. 7(b) shows the cellular uptake of nanoparticles in A549 cells with fluorescein isothiocyanate (FITC) used as a fluorescent marker. Fig. 7(b1) shows there was a definite uptake of Rh-B/F127@β-FeOOH nanospheres by A549 cells with the 24 h incubation time. As shown in Fig. 7(b1), the FITC channel moved to larger intensities compared to the untreated cells, which clearly indicated that Rh-B/F127@β-FeOOH nanoparticles were largely taken up by A549 cells after 24 h treatment.

3.8.3 Cell cycle analysis. The cell cycle advanced through various stages, including G0 (the resting phase), G1 (the gap phase following the previous cell division), S (the phase dedicated to synthesizing nucleotides and proteins for the next division, including DNA replication), G2 (second gap phase), and M (phase focused on kinetic cell division). It has been reported that the checkpoints in G1 and G2 have a significant impact on the control of the cell cycle and are involved in regulating the processes of entering the S and M phases.[66]

FACSVerse cytometry is a capable method to verify the ratio of a cell population in various phases, such as Go/G1, S, and G2/M, by performing quantitative measurements of the nuclear DNA content in each cell cycle. In our study, propidium iodide (PI) was used to stain the nuclear DNA without disturbing the function of the nucleus. Fig. 7(c1)–(c3) show the cell cycle distribution for the untreated and treated A549 cells measured at 24 h incubation. The quantitative results (histogram) for cell cycle arrest are summarized in Fig. 7(c3). As shown in Fig. 7(c1), the cell cycle analysis indicated that the untreated cells exhibited a distribution of 52.68% in G1/G0, 22.97% in G2/M, and 22.78% in the S phase, respectively. Treatment with the Rh-B/F127@β-FeOOH nanospheres induced a significant accumulation of cells in the S phase (increasing from 22.78% to

27.77%), along with a decrease in G2/M population (decreasing from 22.97% to 15.54%). Notably, the G0/G1 phase exhibited minimal changes (Fig. 7(c2)). These findings indicated that the Rh-B/F127@β-FeOOH nanospheres could impair A549 cell proliferation by inducing S-phase cycle arrest, resulting in a reduced G2/M phase population.

3.8.4 Rh-B/F127@β-FeOOH nanospheres-induced ROS generation. The amount of intracellular ROS formation in the A549 cells upon interaction with Rh-B/F127@β-FeOOH nanospheres was determined using DCFH-DA, an oxidation-sensitive fluorogenic marker of ROS in live cells. There was a correlation between the fluorescence intensity and the quantity of ROS produced in the cells. As illustrated in Fig. 8(a2) and (a3), the intracellular ROS generation produced by Rh-B/F127@β-FeOOH nanoparticles demonstrated that there were increasing intracellular ROS levels compared to the control cell levels (Fig. 8(a1)). According to this study, A549 cells treated with Rh-B/F127@β-FeOOH nanospheres showed increased fluorescence at the IC$_{50}$ concentration. With a possible connection to the overproduction of ROS, cytotoxicity effects may be exerted over the induction of oxidative stress and apoptosis. These results suggest that the increased fluorescence intensity found in the A549 cells treated with Rh-B/F127@β-FeOOH nanospheres could be related to the increased production of ROS, as illustrated in Fig. 8(a3). Therefore, it is clear that the generation of ROS plays a crucial role in β-FeOOH-induced apoptosis in A549 cells. This supports the hypothesis that oxidative stress and apoptosis may play roles in the cytotoxicity effects of these nanospheres. Additional research is required to fully understand the mechanisms underlying this association and its potential implications for therapeutic applications.

One of the main mechanisms of cell death brought on by nanoparticles-induced oxidative stress has been identified as apoptosis. Among the various apoptotic pathways, the intrinsic mitochondrial apoptotic pathway has been found to play a pivotal role in nanoparticles-induced cell death since mitochondria are one of the major target organelles for nanoparticles-induced oxidative stress. The overproduction of ROS levels reduces the ROS–antioxidant equilibrium and initiates cell death by apoptosis. Previous literature has indicated that an increase in the intracellular free iron levels affects the normal ROS–antioxidant balance by promoting ROS production through Fenton and/or Haber–Weiss reactions.[67]

Until now, numerous iron-based nanomaterials have been developed as Fenton agents. The Fenton reaction is commonly associated with Fe^{2+} or Fe^{3+}, which can produce hydroxyl radical (˙OH) through peroxidase mimicking the catalytic decomposition of H$_2$O$_2$. It is well known that superoxide-driven Fenton reactions and/or Haber–Weiss reactions provide an effective method for generating OH˙ in A549 cells. If superoxide and H$_2$O$_2$ are generated in cells, they might induce significant energy and selective cancer cell death. In this catalytic reaction, the superoxide, O$_2$˙$^{-}$ serves as a precursor for H$_2$O$_2$ and a reductant for Fe^{3+} (Fe^{3+} → Fe^{2+}). Finally, the Fenton reaction generates hydroxyl radicals (˙OH) from H$_2$O$_2$ through the oxidation of Fe^{2+} (Fe^{2+} → Fe^{3+}) (as shown in Fig. 8(d)).[67] Generally, in living systems, a "leakage" of electrons from the
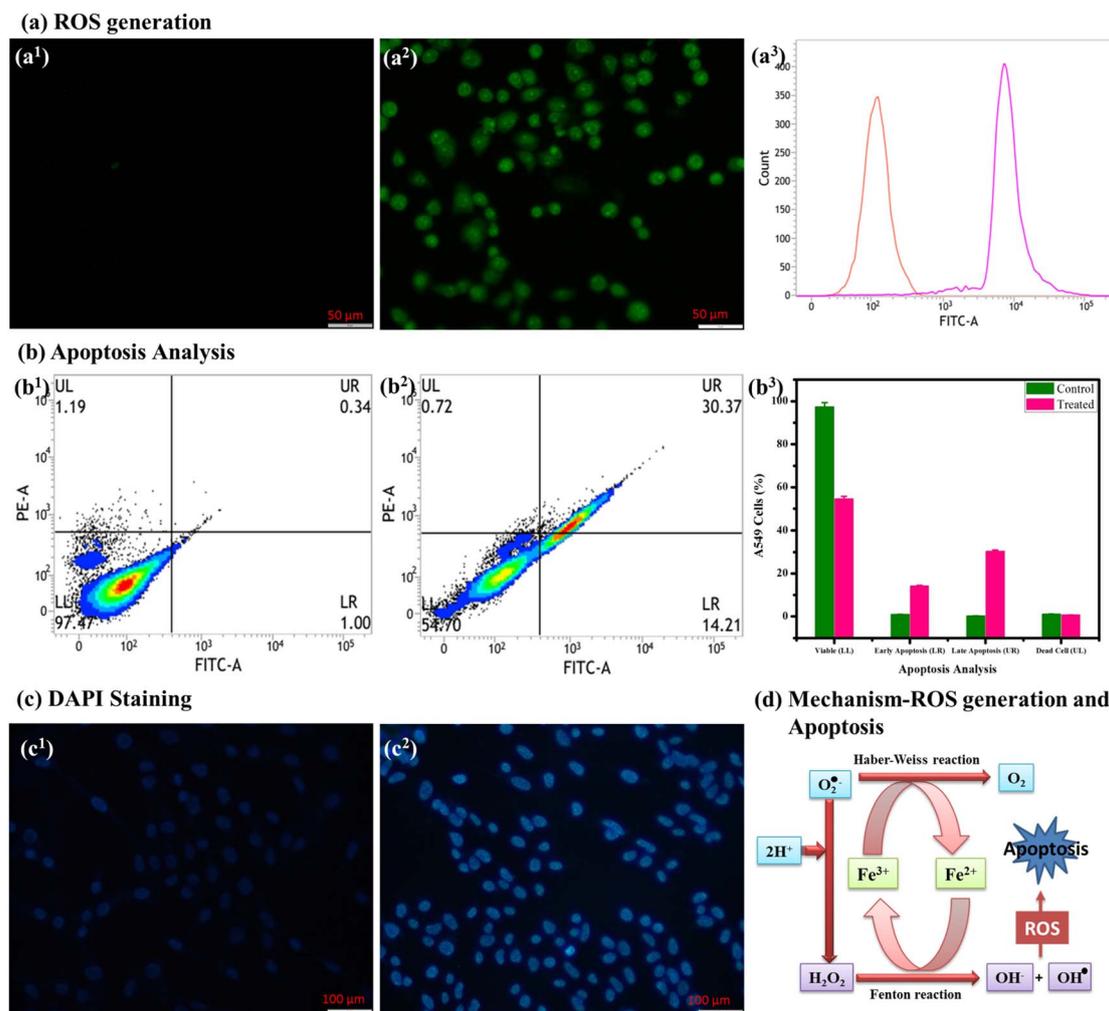
Fig. 8 Apoptosis study. (a) Rh-B/F127@β-FeOOH nanospheres-induced ROS generation in A549 cells: (a¹) control, (a²) ROS induced by nanoparticles, (a³) FCM analysis of intracellular ROS using a DFCH-DA probe. (b) Evaluation of apoptosis in A549 cells using the annexin-V/dead cell assay: A549 cells were treated with Rh-B/F127@β-FeOOH nanospheres for 24 h and apoptosis was assayed *via* flow cytometry using the annexin-V/dead cell assay; (b¹) control, (b²) treated, and (b³) histogram showing % cell death. (c) Morphology of A549 cell nuclei observed using DAPI staining: (c¹) control, and (c²) treated cells. DAPI images were recorded using laser light excitation at 360 nm. The scale bars represent 100 μm. (d) Proposed mechanism for ROS generation and apoptosis cell death by the overproduction of ROS generation (generation of OH^- and $^{\bullet}OH^-$ radicals through Fenton and/or Haber–Weiss reactions).

electron-transport chain produces superoxide radicals and hydrogen peroxide in both intracellular and extracellular volumes. The overproduction of ROS through β-FeOOH nanospheres leads to mitochondria membrane destruction and DNA fragmentation and thereby induces cancer cell apoptosis. The mechanism in the present study allows efficient tumor-specific treatment without producing significant side effects in healthy cells (IC_{50} value > 500 μg mL^{-1}).

$$Fe^{3+} + O_2^{\bullet -} \rightarrow Fe^{2+} + O_2 \text{ (Haber–Weiss reaction)}$$

$$Fe^{2+} + H_2O_2 \rightarrow Fe^{3+} + OH^- + {}^{\bullet}OH^- \text{ (Fenton reaction)}$$

3.8.5 Apoptosis cell death. Further, the percentage of apoptosis was measured by annexin-V analysis using flow cytometry. As shown in Fig. 8(b1)–(b3), the apoptotic cell profiles showed a quadratic format with four different stages: lower-left quadrant (% of live cells), lower-right quadrant (% of early apoptosis), upper-left quadrant (% of late apoptosis), and upper-right quadrant (% of necrosis), respectively.

The annexin-V assay demonstrated a marked induction of late apoptosis in A549 cells treated with Rh-B/F127@β-FeOOH nanospheres for 24 h. Specifically, the percentage of late apoptotic cells increased from 0.34% (untreated controls) to 30.37% at the IC_{50} concentration, indicating a late apoptotic effect (Fig. 8(c)). The histogram in Fig. 8(c3) shows the quantification% of cell death.

3.8.6 DAPI staining. Rh-B/F127@β-FeOOH nanospheres-induced nuclear fragmentation in A549 cells was investigated by DAPI fluorescent nuclear staining. The findings are presented in Fig. 8(c1) and (c2), where the untreated cell nuclei appeared normal and smooth with low fluorescence, whereas

the treated cells showed obvious changes in chromatin condensation, DNA fragmentation, and membrane blebbing.[68] The above results suggest that the nanoparticles caused cell death. In addition, the distinct morphology of the treated cells showed bright images owing to the fluorescence effect, which indicated that the nanoparticles may be undergoing later stages of apoptosis, supporting the findings from the apoptosis study.

3.8.7 Cellular morphology analysis by dual AO/EtBr staining assay. As shown in Fig. 9, flow cytometry analysis demonstrated the nanospheres-induced cell apoptosis death in A549 cells. The effects of Rh-B/F127@β-FeOOH nanospheres-induced apoptosis were further visualized using AO/EtBr dual staining. Untreated and treated A549 cells were stained with AO/EtBr for 15 min, and subsequently, the cells were rinsed in PBS to remove the non-internalized nanoparticles and then imaged using fluorescence microscopy. Fig. 9(a) and (b) present the fluorescence images of untreated and β-FeOOH nanospheres-induced apoptosis A549 cell death with AO/EtBr dual staining.

Fig. 9(a) shows the bright field images of A549 cell lines without the incubation of nanoparticles, wherein their cellular boundaries are clearly visible. Fig. 9(b) shows the A549 cells with Rh-B/F127@β-FeOOH nanospheres visualized under a fluorescence microscope, wherein the results showed green, yellow-orange, and red emissions that originated from the live cell membrane and early-stage and later-stage apoptosis of A549 cells, respectively. Green fluorescence appeared in the normal viable control cells because AO can only bind to viable cell membranes. The yellow-orange-colored bodies originated from early apoptosis, which may be due to nuclear shrinkage and blebbing (condensed chromatin), whereas red fluorescence showed the later-stage apoptotic cells. The above results verified the Rh-B/F127@β-FeOOH nanospheres-induced apoptosis of A549 cells, which occurred for any one of the following reasons: (i) changes in chromatin condensation, (ii) fragmented nuclei, and (ii) membrane blebbing.[69]

3.9 Antioxidant activity of Rh-B/F127@β-FeOOH nanorods

Reactive oxygen species (ROS) are unfavorable by-products of cellular respiration that are essential for cell signaling but can also lead to oxidative damage in living cells. ROS are molecules, ions, and free radicals that are extremely active due to their unpaired valence shell electrons. An excess of ROS in the body has been linked to a number of disorders, such as cancer, aging, cataracts, diabetic milieus, cardiovascular disease, and cognitive dysfunction. Antioxidants are crucial in stopping free radicals before they damage cells and other biological targets and for preventing a number of diseases because of their capability to scavenge free radicals.

The antioxidant activity of iron-based nanoparticles, like Fe_2O_3 and Fe_3O_4 NPs, has been well-established in previous studies[70,71] and is rooted in their capacity to neutralize free radicals through hydrogen atom transfer or electron donation. This mechanism protects biomolecules from oxidative damage.

Based on the above literature, the antioxidant capacities of Rh-B/F127@β-FeOOH nanorods showed potential free-radical-scavenging activity against all three separate assays: DPPH, ferric reducing antioxidant power (FRAP), and reducing power assay (RP), with each of them performed at different concentrations from 100 to 500 μg mL^{-1} and the results are depicted in Fig. 10(a)–(c). Ascorbic acid was used as a positive control in the same concentration range.

The antioxidant activity of Rh-B/F127@β-FeOOH nanorods was assessed using the 1,1-diphenyl-2-picryl-hydrazyl (DPPH) scavenging assay, as shown in Fig. 10(a). The DPPH assay provided a rapid and straightforward method for evaluating the nanorods' free-radical-scavenging capacity. The antioxidant activity is attributed to electron transfer from oxygen atoms on the particle surface to the nitrogen atom of DPPH molecules, resulting in stable molecule formation.[72] Fig. 10(a) illustrates the dose-dependent (100–500 μg mL^{-1}) DPPH-scavenging activity against Rh-B/F127@β-FeOOH nanorods. The results exhibited their potent inhibitory action and dose-dependent
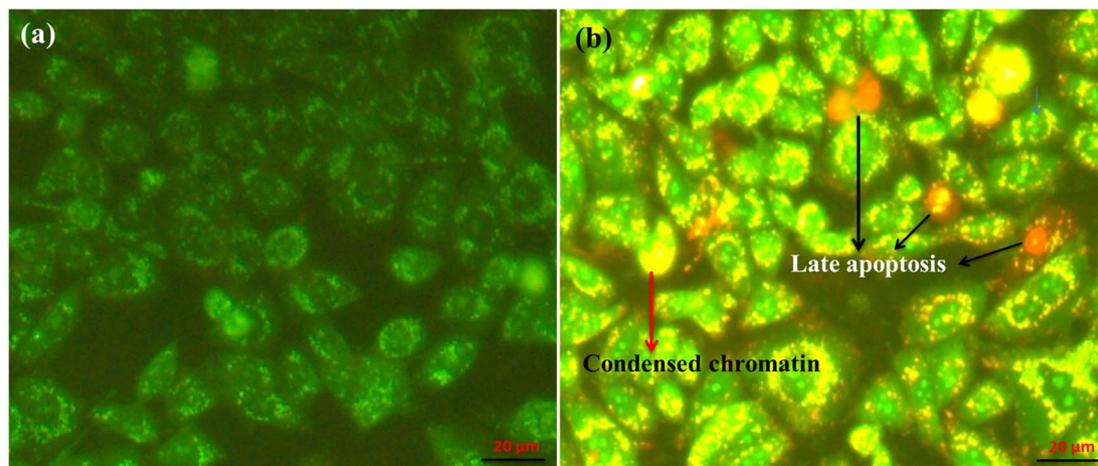

Fig. 9 Fluorescence images of A549 cells stained with acridine orange/ethidium bromide (AO/EB). (a) Untreated cells (control); (b) cells incubated with Rh–B/F127@β-FeOOH nanoparticles. The cells were observed at an excitation wavelength of 480 nm. The bright-green emissions originated from the live cells (untreated cells), while yellow–orange indicated early-stage apoptotic cells. Red emissions originated from late apoptosis. The scale bars represent 20 μm.

free-radical-scavenging capability. The values of the DPPH radical scavenging efficiencies against Rh-B/F127@β-FeOOH nanorods were 62.42% (100 μg mL^{-1}), 66.64% (150 μg mL^{-1}), 70.86% (200 μg mL^{-1}), 81.06% (300 μg mL^{-1}), and 88.56% (500 μg mL^{-1}). The free-radical-scavenging activity of Rh-B/F127@β-FeOOH nanorods was slightly higher compared with the standard (52.4–71.1%) inhibition. Therefore, our results demonstrate that Rh-B/F127@β-FeOOH nanorods have substantial antioxidant potential, consistent with or even exceeding that reported in previous studies.

The ability of an antioxidant to contribute an electron can be quantified by the reducing power assay. However, the reducing power assay may not accurately measure the overall antioxidant capacity of a compound as it only evaluates its ability to donate electrons, neglecting other important aspects, such as its stability and ability to neutralize free radicals. This assay relies on the interaction of samples with potassium ferricyanide (Fe^{3+}) to generate potassium ferrocyanide (Fe^{2+}). Subsequently, a reaction with ferric chloride (FeCl$_3$) results in the formation of a ferric–ferrous complex, exhibiting a maximum absorbance at 700 nm, as illustrated in Fig. 10(b). For the measurement of the reductive ability, we investigated Fe^{3+} to Fe^{2+} transformation in the presence of β-FeOOH NRs following the standard method.[73]

The reducing capacity of a compound may serve as a significant indicator of its potential antioxidant activity. It was observed that, the antioxidant activity and the reducing power of β-FeOOH NRs increased with their increasing concentration.

The FRAP assay can evaluate antioxidant potency by measuring the reduction of ferric ions (Fe^{3+}) to ferrous ions (Fe^{2+}) *via* electron transfer.[74] This process, described by the reaction Fe^{3+} + e$^-$ → Fe^{2+}, was significantly enhanced by the presence of β-FeOOH nanorods. The ferric reducing power of the Rh-B/F127@β-FeOOH nanorods was evaluated using the FRAP assay. Fig. 10(c) shows a dose-dependent (100–500 μg mL^{-1}) increase in the reducing power was observed. The obtained results showed significant inhibition at 500 μg mL^{-1}. Notably, the Rh-B/F127@β-FeOOH nanorods exhibited a superior ferric-ions-reducing capacity compared to ascorbic acid (vitamin C) at 500 μg mL^{-1}, indicating their robust antioxidant potential.

The above results strongly suggest that the β-FeOOH nanorods have a strong antioxidant capacity and could potentially be used as a natural alternative to ascorbic acid in certain applications. Further analyses are required to examine the underlying mechanisms behind this enhanced reducing power and to

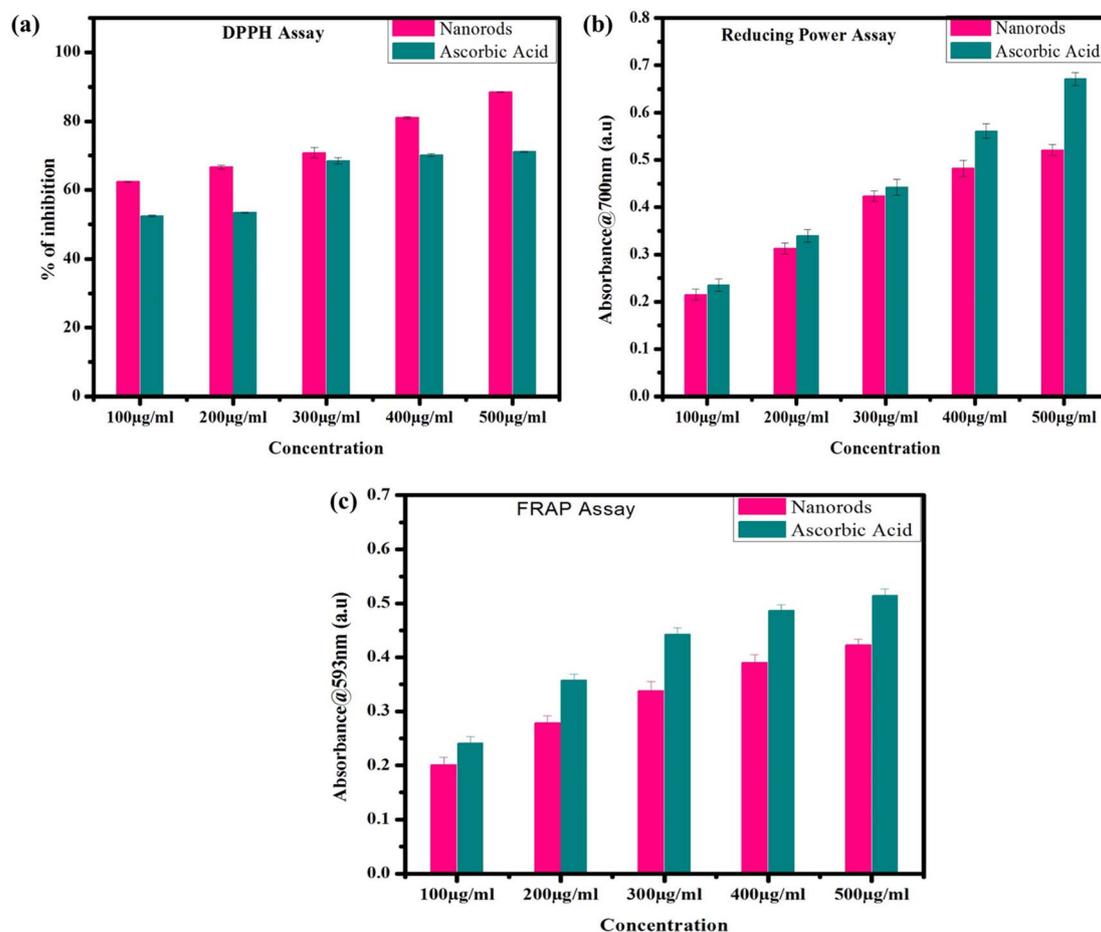Fig. 10 Antioxidant activity of Rh-B/F127@β-FeOOH nanorods. (a) DPPH assay, (b) reducing power assay, and (c) FRAP assay. The antioxidant activity of β-FeOOH nanorods was found to increase with the increase in concentration from 100 to 500 mg mL^{-1}.

explore the potential benefits of using β-FeOOH nanorods in various industries and applications.

4. Conclusions

In summary, dye/polymer matrix-stabilized β-FeOOH nanomaterials were developed and characterized and showed potential to serve as therapeutic agents. The as-prepared nanomaterials were characterized using various techniques, including FT-IR, UV-Vis, PL, XRD, HR-TEM, and XPS. The hydrothermally synthesized Rh-B/F127@β-FeOOH nanospheres produced multi-colored emissions. The XRD results provided additional confirmation of the crystal structure. The oxidative states and presence of various elements were confirmed by XPS spectroscopy. The obtained β-FeOOH nanomaterials showed rod-like and spherical-like morphologies, as confirmed by HR-TEM analysis. The cytotoxicity activity of β-FeOOH nanospheres against A549 cells was analyzed by MTT assay. Flow cytometry was used to analyze the reactive oxygen species (ROS) generation and apoptotic cell death caused by the β-FeOOH nanospheres. The induction of apoptosis in A549 cells was revealed by annexin-V with propidium iodide (PI) and DAPI staining. From the cell cycle analysis, it was observed that the β-FeOOH nanospheres blocked the cell cycle development of A549 cells in the S phases supported by an increase in the S-phase cell population. The antioxidant activities of the nanorods were confirmed by different assays, such as DPPH, FRAP, and PFRAP. The results showed that the nanorods have a high scavenging activity against free radicals. Overall, the present study suggests that the synthesized Rh-B/F127@β-FeOOH nanoparticles are attractive and efficient candidates for various biomedical applications, including anticancer and antioxidant activities.

Data availability

The authors confirm that the data will be available on request.

Author contributions

CNM, MA: construction plan, writing-original draft preparation, graphical and software work. PAP: cytotoxicity interpretation and anticancer activity. PRK, JK: XPS and HR-TEM analysis. GMR, SMKT, LG, MKH: visualization and format checking. KP: graphical and software work. All authors have given approval to the final version of the manuscript.

Conflicts of interest

We declare that we have no known competing financial interests or personal relationships that could have appeared to influence the work reported in this paper.

Acknowledgements

References

1 C. Bae, H. Kim, Y.-M. Kook, C. Lee, C. Kim, C. Yang, M. H. Park, Y. Piao, W.-G. Koh and K. Lee, Induction of ferroptosis using functionalized iron-based nanoparticles for anti-cancer therapy, *Mater. Today Bio*, 2022, **17**, 100457.

2 H. Zhao, Y. Dong, P. Jiang, G. Wang and J. Zhang, Highly dispersed CeO_2 on TiO_2 nanotube: a synergistic nanocomposite with superior peroxidase-like activity, *ACS Appl. Mater. Interfaces*, 2015, **7**, 6451–6461.

3 Z. Zhang, J. Hao, W. Yang, B. Lu, X. Ke, B. Zhang and J. Tang, Porous Co_3O_4 nanorods–reduced graphene oxide with intrinsic peroxidase-like activity and catalysis in the degradation of methylene blue, *ACS Appl. Mater. Interfaces*, 2013, **5**, 3809–3815.

4 M. Hu, K. Korschelt, P. Daniel, K. Landfester, W. Tremel and M. B. Bannwarth, Fibrous nanozyme dressings with catalase-like activity for H_2O_2 reduction to promote wound healing, *ACS Appl. Mater. Interfaces*, 2017, **9**, 38024–38031.

5 J. A. Champion, Y. K. Katare and S. Mitragotri, Particle shape: a new design parameter for micro- and nanoscale drug delivery carriers, *J. Controlled Release*, 2007, **121**, 3–9.

6 D. Chen, W. Wei, R. Wang, J. Zhu and L. Guo, α-Fe_2O_3 nanoparticles anchored on graphene with 3D quasi-laminated architecture: in situ wet chemistry synthesis and enhanced electrochemical performance for lithium ion batteries, *New J. Chem.*, 2012, **36**, 1589–1595.

7 Y. Yang, M. Liu, H. Zhu, Y. Chen, G. Mu, X. Liu and Y. Jia, Preparation, characterization, magnetic property, and Mössbauer spectra of the β-FeOOH nanoparticles modified by nonionic surfactant, *J. Magn. Magn. Mater.*, 2008, **320**, 132–136.

8 N. G. Holm, New evidence for a tubular structure of β-iron(III) oxide hydroxide-akaganéite, *Origins Life Evol. Biospheres*, 1985, **15**, 131–139.

9 H. Morimoto, K. Takeno, Y. Uozumi, K. I. Sugimoto and S. I. Tobishima, Synthesis of composite electrode materials of FeOOH-based particles/carbon powder and their high-rate charge–discharge performance in lithium cells, *J. Power Sources*, 2011, **196**, 6512–6516.

10 J. Cai, J. Liu, Z. Gao, A. Navrotsky and S. L. Suib, Synthesis and anion exchange of tunnel structure akaganeite, *Chem. Mater.*, 2001, **13**, 4595–4602.

11 M. Mohapatra, L. Mohapatra, S. Anand and B. K. Mishra, One-Pot Synthesis of High Surface Area Nano-Akaganeite Powder and Its Cation Sorption Behavior, *J. Chem. Eng. Data*, 2010, **55**, 1486–1491.

12 T. Wang, P. Zhang, S. Ni, Y. Huang, K. Qiu, J. Li, M. Zhang, H. Yin and J. Li, Synthesis of nano-akaganeite powder and its chromium adsorption behaviour, *Ferroelectrics*, 2019, **540**, 184–192.

13 E. A. Deliyanni, D. N. Bakoyannakis, A. I. Zouboulis, K. A. Matis and L. Nalbandian, Akaganeite-type beta-FeO(OH) nanocrystals: preparation and characterization, *Microporous Mesoporous Mater.*, 2001, **42**, 49–57.

14 L. Zeng, W. Ren, J. Zheng, A. Wu and P. Cui, Synthesis of water-soluble FeOOH nanospindles and their performance

for magnetic resonance imaging, *Appl. Surf. Sci.*, 2012, **258**, 2570–2575.

15 Y. X. Zhang and Y. Jia, A facile solution approach for the synthesis of akaganéite (β-FeOOH) nanorods and their ion-exchange mechanism toward As (V) ions, *Appl. Surf. Sci.*, 2014, **290**, 102–106.

16 X. Zhang, J. Ge, B. Lei, Y. Xue and Y. Du, High quality β-FeOOH nanostructures constructed by a biomolecule-assisted hydrothermal approach and their pH-responsive drug delivery behaviours, *CrystEngComm*, 2015, **17**, 4064–4069.

17 W. R. Richmond, J. M. Cowley, G. M. Parkinson and M. Saunders, An electron microscopy study of β-FeOOH (akaganéite) nanorods and nanotubes, *CrystEngComm*, 2006, **8**, 36–40.

18 M. Tadic, I. Milosevic, S. Kralj, M. Mbodji and L. Motte, Silica-Coated and Bare Akaganeite Nanorods: Structural and Magnetic Properties, *J. Phys. Chem. C*, 2015, **119**, 13868–13875.

19 Y. Xiong, Y. Xie, S. Chen and Z. Li, Fabrication of self-supported patterns of aligned β-FeOOH nanowires by a low-temperature solution reaction, *Chem.–Eur. J.*, 2003, **9**, 4991–4996.

20 K. Cho, B. Shin, H. K. Park, B. G. Cha and J. Y. Kim, Size-controlled synthesis of uniform akaganeite nanorods and their encapsulation in alginate microbeads for arsenic removal, *RSC Adv.*, 2014, **4**, 21777–21781.

21 M. Nesterova, J. Moreau and J. F. Banfield, Model biomimetic studies of templated growth and assembly of nanocrystalline FeOOH, *Geochim. Cosmochim. Acta*, 2003, **67**, 1177–1187.

22 Y. Hao, X. Gao and P. W. Chen, One-step synthesis of FeO(OH) nanoparticles by electric explosion of iron wire underwater, *Def. Technol.*, 2022, **18**, 133–139.

23 H. Xiong, Y. Liao, L. Zhou, Y. Xu and S. Wang, Biosynthesis of Nanocrystal Akaganéite from FeCl$_2$ Solution Oxidized by *Acidithiobacillus ferrooxidans* Cells, *Environ. Sci. Technol.*, 2008, **42**, 4165–4169.

24 N. Zhang, Q. Sheng, Y. Zhou, S. Dong and J. Zheng, Synthesis of FeOOH@PDA-Ag nanocomposites and their application for electrochemical sensing of hydrogen peroxide, *J. Electroanal. Chem.*, 2016, **781**, 315–321.

25 Y. X. Yang, M. L. Liu, H. Zhu, Y. R. Chen, G. J. Mu, X. N. Liu and Y. Q. Jia, Preparation, characterization, magnetic property, and Mossbauer spectra of the β-FeOOH nanoparticles modified by nonionic surfactant, *J. Magn. Magn. Mater.*, 2008, **320**, 132–136.

26 X. Chen, Y. Zeng, Z. Chen, S. Wang, C. Xin, L. Wang, C. Shi, L. Lu and C. Zhang, Synthesis and electrochemical property of FeOOH/graphene oxide composites, *Front. Chem.*, 2020, **8**, 328.

27 T. T. V. Phan, N. Q. Bui, S. W. Cho, S. Bharathiraja, P. Manivasagan, M. S. Moorthy, S. Mondal, C. S. Kim and J. Oh, Photoacoustic imaging-guided photothermal therapy with tumor-targeting HA-FeOOH@PPy nanorods, *Sci. Rep.*, 2018, **8**, 8809.

28 X.-L. Shi, G.-J. Mao, X.-B. Zhang, H.-W. Liu, Y.-J. Gong, Y.-X. Wu, L.-Y. Zhou, J. Zhang and W. Tan, Rhodamine-based fluorescent probe for direct bio-imaging of lysosomal pH changes, *Talanta*, 2014, **130**, 356–362.

29 H. Liu, Y. Wang, H. Li, Z. Wang and D. Xu, Luminescent rhodamine B doped core-shell silica nanoparticle labels for protein microarray detection, *Dyes Pigm.*, 2013, **98**, 119–124.

30 Y.-H. Zhu, J.-L. Wang, H.-B. Zhang, M. I. Khan, X.-J. Du and J. Wang, Incorporation of a rhodamine B conjugated polymer for nanoparticle trafficking both *in vitro* and *in vivo*, *Biomater. Sci.*, 2019, **7**, 1933–1939.

31 J. Kennedy, E. Larrañeta, M. T. C. McCrudden, C. M. McCrudden, A. J. Brady, S. J. Fallows, H. O. McCarthy, A. Kissenpfennig and R. F. Donnelly, *In vivo* studies investigating biodistribution of nanoparticle-encapsulated rhodamine B delivered *via* dissolving microneedles, *J. Controlled Release*, 2017, **265**, 57–65.

32 X. Wang, X.-Q. Chen, H.-S. Peng, X.-F. Wei, X.-J. Wang, K. Cheng, Y.-A. Liu and W. Yang, Facile synthesis of polypyrrole-rhodamine B nanoparticles for self-monitored photothermal therapy of cancer cells, *J. Mater. Chem. B*, 2020, **8**, 1033–1039.

33 C.-Y. Hsu and Y.-L. Liu, Rhodamine B-anchored silica nanoparticles displaying white-light photoluminescence and their uses in preparations of photoluminescent polymeric films and nanofibers, *J. Colloid Interface Sci.*, 2010, **350**, 75–82.

34 C. Jian, C. Gong, S. Wang, S. Wang, X. Xie, Y. Wei and J. Yuan, Multifunctional comb copolymer ethyl cellulose-g-poly(ε-caprolactone)-rhodamine B/folate: synthesis, characterization and targeted bonding application, *Eur. Polym. J.*, 2014, **55**, 235–244.

35 J. Qiao, P. Dong, X. Mu, L. Qi and R. Xiao, Folic acid-conjugated fluorescent polymer for up-regulation folate receptor expression study *via* targeted imaging of tumor cells, *Biosens. Bioelectron.*, 2016, **78**, 147–153.

36 A. Cabana, A. Ait-Kadi and J. Juhász, Study of the gelation process of polyethylene oxide–polypropylene oxide – polyethylene oxide copolymer (poloxamer 407) aqueous solutions, *J. Colloid Interface Sci.*, 1997, **19**, 307–312.

37 H. Vu-Quang, M. S. Vinding, T. Nielsen, M. G. Ullisch, N. C. Nielsen, D. T. Nguyen, *et al.*, Pluronic F127-folate coated super paramagnetic iron oxide nanoparticles as contrast agent for cancer diagnosis in magnetic resonance imaging, *Polymers*, 2019, **11**, 743.

38 J. Gilbert, J. Hadgraft, A. Bye and L. Brookes, Drug release from Pluronic F-127 gels, *Int. J. Pharm.*, 1986, **32**, 223–228.

39 Y. Kadama, U. Yerramillia and A. Bahadur, Solubilization of poorly water-soluble drug carbamezapine in Pluronic® micelles: effect of molecular characteristics, temperature and added salt on the solubilizing capacity, *Colloids Surf., B*, 2009, **72**, 141–147.

40 Z. Wei, J. Hao, S. Yuan, Y. Li, W. Juan, X. Sha and X. Fang, Paclitaxel-loaded Pluronic P123/F127 mixed polymeric micelles: formulation, optimization and *in vitro* characterization, *Int. J. Pharm.*, 2009, **376**, 176–185.

41 T. Sakai and P. Alexandridis, Single-Step Synthesis and Stabilization of Metal Nanoparticles in Aqueous Pluronic Block Copolymer Solutions at Ambient Temperature, *Langmuir*, 2004, **20**, 8426–8430.

42 Y. Wu, J. Liu, J. Ma, Y. Liu, Y. Wang and D. Wu, Ratiometric Nanothermometer Based on Rhodamine Dye-Incorporated F127-Melamine-Formaldehyde Polymer Nanoparticle: Preparation, Characterization, Wide-Range Temperature Sensing, and Precise Intracellular Thermometry, *ACS Appl. Mater. Interfaces*, 2016, **8**, 14396–14405.

43 D. Chowrasia, C. Karthikeyan, L. Choure, M. Gupta, M. Arshad and P. Trivedi, Synthesis, characterization and anticancer activity of some fluorinated 3,6-diaryl-[1,2,4]triazolo[3,4-b][1,3,4]thiadiazoles, *Arabian J. Chem.*, 2017, **10**, S2424–S2428.

44 S. Karthik, R. Sankar, K. Varunkumar and V. Ravikumar, Romidepsin induces cell cycle arrest, apoptosis, histone hyperacetylation and reduces matrix metalloproteinases 2 and 9 expression in bortezomib sensitized non-small cell lung cancer cells, *Biomed. Pharmacother.*, 2014, **68**, 327–334.

45 A. Serpen, E. Capuano, V. Fogliano and V. Gökmen, A new procedure to measure the antioxidant activity of insoluble food components, *J. Agric. Food Chem.*, 2007, **55**, 7676–7681.

46 R. Pulido, L. Bravo and F. Saura-calixto, Antioxidant activity of dietary polyphenols as determined by a modified ferric reducing/antioxidant power assay, *J. Agric. Food Chem.*, 2000, **44**, 3396–3402.

47 I. E. F. Benzie and J. J. Strain, The ferric reducing ability of plasma (FRAP) as a measure of antioxidant power: the FRAP assay, *Anal. Biochem.*, 1996, **239**, 70–76.

48 A. Ghanbariasad, S. M. Taghizadeh, P. L. Show, S. Nomanbhay, A. Berenjian, Y. Ghasemi and A. Ebrahiminezhad, Controlled synthesis of iron oxyhydroxide (FeOOH) nanoparticles using secretory compounds from *Chlorella vulgaris* microalgae, *Bioengineered*, 2019, **10**, 390–396.

49 C. Luna, M. Ilyn, V. Vega, V. M. Prida, J. González, R. Mendoza-Reséndez, M. de Lardizabal and S. Sebastián, Size distribution and frustrated antiferromagnetic coupling effects on the magnetic behavior of ultrafine akaganéite (β-FeOOH) nanoparticles, *J. Phys. Chem. C*, 2014, **118**, 21128.

50 S. Bashir, R. W. McCabe, C. Boxall, M. S. Leaver and D. Mobbs, Synthesis of α- and β-FeOOH iron oxide nanoparticles in non-ionic surfactant medium, *J. Nanopart. Res.*, 2009, (11), 701–706.

51 V. Renuga, C. Neela Mohan, M. S. M. Jaabir, P. A. Prakash and M. Navaneethan, Synthesis and Surface Passivation of CuInS₂/MnS/ZnS Core–Multishell Nanocrystals, their Optical, Structural, and Morphological Characterization, and their Bioimaging Applications, *Ind. Eng. Chem. Res.*, 2018, **57**, 15703–15721.

52 A. Lassoued, B. Dkhil, A. Gadri and S. Ammar, Control of the shape and size of iron oxide (α-Fe₂O₃) nanoparticles synthesized through the chemical precipitation method, *Results Phys.*, 2017, **7**, 3007–3015.

53 I. P. Pozdnyakov, A. V. Kolomeets, V. F. Plyusnin, A. A. Melnikov, V. O. Kompanets, S. V. Chekalin,

N. Tkachenko and H. Lemmetyinen, Photophysics of Fe(III)–tartrate and Fe(III)–citrate complexes in aqueous solutions, *Chem. Phys. Lett.*, 2012, **530**, 45–48.

54 X. S. Xu, T. V. Brinzari, S. Lee, Y. H. Chu, L. W. Martin, A. Kumar, S. McGill, R. C. Rai, R. Ramesh, V. Gopalan, S. W. Cheong and J. L. Musfeldt, Optical properties and magnetochromism in multiferroic BiFeO₃, *Phys. Rev. B: Condens. Matter Mater. Phys.*, 2009, **79**, 134425.

55 J. H. Jung, M. Matsubara, T. Arima, J. P. He, Y. Kaneko and Y. Tokura, Optical Magnetoelectric Effect in the Polar GaFeO₃ Ferrimagnet, *Phys. Rev. Lett.*, 2004, **93**, 037403.

56 M. F. Kircher, U. Mahmood, R. S. King, R. Weissleder and L. Josephson, A multimodal nanoparticle for preoperative magnetic resonance imaging and intraoperative optical brain tumor delineation, *Cancer Res.*, 2003, **63**, 8122–8125.

57 G. Park, Y. –I. Kim, Y. H. Kim, M. Park, K. Y. Jang, H. Song and K. M. Nam, Preparation and phase transition of FeOOH nanorods: strain effects on catalytic water oxidation, *Nanoscale*, 2017, **9**, 4751–4758.

58 T. Yamashita and P. Hayes, Analysis of XPS spectra of Fe²⁺ and Fe³⁺ ions in oxide materials, *Appl. Surf. Sci.*, 2008, **254**, 2441–2449.

59 F. Yang, S. Zhang, H. Li, S. Li, K. Cheng, J. S. Li and D. C. W. Tsang, Corn straw-derived biochar impregnated with α-FeOOH nanorods for highly effective copper removal, *Chem. Eng. J.*, 2018, **348**, 191–201.

60 X. Song and J. F. Boily, Variable hydrogen bond strength in akaganeite, *J. Phys. Chem. C*, 2012, **116**, 2303–2312.

61 Y. Li, X. Li, Y. Hao, A. Kakimov, D. Li, Q. Sun, L. Kou, Z. Tian, L. Shao, C. Zhang, J. Zhang and X. Sun, β-FeOOH interlayer with abundant oxygen vacancy toward boosting catalytic effect for lithium sulfur batteries, *Front. Chem.*, 2020, **8**, 309.

62 C. Neela Mohan, V. Renuga and A. Manikandan, Influence of silver precursor concentration on structural, optical and morphological properties of Cu₁₋ₓAgₓInS₂ semiconductor nanocrystals, *J. Alloys Compd.*, 2017, **729**, 407–417.

63 M. Bhushan, Y. Kumar, L. Periyasamy and A. K. Viswanath, Antibacterial applications of α-Fe₂O₃/Co₃O₄ nanocomposites and study of their structural, optical, magnetic and cytotoxic characteristics, *Appl. Nanosci.*, 2018, **8**, 137–153.

64 T. A. Alkinani, F. A. Bajgiran, M. Rezaei, A. M. Maivan, F. J. Golrokh, M. Bejarbaneh, S. R. Mojdehi, S. Gorji, R. Ghasemian, M. D. J. Pustin Sarai, F. Akbari, S. Dehghan, F. Mirzaee, N. H. Abdulrahman and A. Salehzadeh, Evaluation the cytotoxic effect of Fe₃O₄@Glu-gingerol on lung adenocarcinoma cell line (A549) with biological mechanisms, *Heliyon*, 2024, **10**, e23419.

65 S. Das, S. Diyali, G. Vinothini, B. Perumalsamy, B. Gowdhami, T. Ramasamy and B. Biswas, Synthesis, morphological analysis, antibacterial activity of iron oxide nanoparticles and the cytotoxic effect on lung cancer cell line, *Heliyon*, 2020, **6**, 04953.

66 J. A. Pietenpol and Z. A. Stewart, Cell cycle checkpoint signaling: cell cycle arrest *versus* apoptosis, *Toxicology*, 2002, **181–182**, 475–481.

67 M. A. Voinov, J. O. Sosa Pagán, E. Morrison, T. I. Smirnova and A. I. Smirnov, Surface-Mediated Production of Hydroxyl Radicals as a Mechanism of Iron Oxide Nanoparticle Biotoxicity, *J. Am. Chem. Soc.*, 2011, **133**, 35–41.

68 J. Raju, J. M. R. Patlolla, M. V. Swamy and C. V. Rao, Diosgenin, a Steroid Saponin of *Trigonella foenum graecum* (Fenugreek), Inhibits Azoxymethane-Induced Aberrant Crypt Foci Formation in F344 Rats and Induces Apoptosis in HT-29 Human Colon Cancer Cells, *Cancer Epidemiol., Biomarkers Prev.*, 2004, **13**, 1392–1398.

69 S. Y. Choi, N. Yang, S. K. Jeon and T. H. Yoon, Semi-Quantitative Estimation of Cellular SiO_2 Nanoparticles Using Flow Cytometry Combined with X-ray Fluorescence Measurements, *Cytometry*, 2014, **85**, 771–780.

70 S. Majeed, M. Danish, I. M. N. Mohamad, S. H. Sekeri, M. T. Ansari, A. Nanda and G. Ahmad, Bacteria mediated synthesis of iron oxide nanoparticles and their antibacterial, antioxidant, cytocompatibility properties, *J. Cluster Sci.*, 2021, **32**, 1083–1094.

71 A. Bouafia, S. E. Laouini, A. Khelef, M. L. Tedjani and F. Guemari, Effect of ferric chloride concentration on the type of magnetite (Fe_3O_4) nanoparticles biosynthesized by aqueous leaves extract of artemisia and assessment of their antioxidant activities, *J. Cluster Sci.*, 2021, **32**, 1033–1041.

72 N. Mohamed, O. E. Hessen and H. S. Mohammed, Thermal stability, paramagnetic properties, morphology and antioxidant activity of iron oxide nanoparticles synthesized by chemical and green methods, *Inorg. Chem. Commun.*, 2021, **128**, 108–572.

73 M. Ullah, D.-S. Kim and K.-H. Park, Evaluating antioxidant activity of phenolic mediated Fe_3O_4 nanoparticles using *Usnea longissima* methanol extract, *Results Chem.*, 2022, **4**, 10066.

74 N. A. Zakariya, S. Majeed, W. Hafizah and W. Jusof, Investigation of antioxidant and antibacterial activity of iron oxide nanoparticles (IONPS) synthesized from the aqueous extract of *Penicillium* spp, *Sens. Int.*, 2022, **3**, 100164.